

Dominating Vertical Collaborative Learning Systems

Qi Pang, Yuanyuan Yuan, Shuai Wang
 The Hong Kong University of Science and Technology
 Hong Kong SAR
 {qpangaa,yyuanaq,shuaiw}@cse.ust.hk

ABSTRACT

Vertical collaborative learning system also known as vertical federated learning (VFL) system has recently become prominent as a concept to process data distributed across many individual sources without the need to centralize it. Multiple participants collaboratively train models based on their local data in a privacy-preserving manner. To date, VFL has become a de facto solution to securely learn a model among organizations, allowing knowledge to be shared without compromising privacy of any individual organizations.

Despite the prosperous development of VFL systems, we find that certain inputs of a participant, named adversarial dominating inputs (ADIs), can dominate the joint inference towards the direction of the adversary’s will and force other (victim) participants to make negligible contributions, losing rewards that are usually offered regarding the importance of their contributions in collaborative learning scenarios.

We conduct a systematic study on ADIs by first proving their existence in typical VFL systems. We then propose gradient-based methods to synthesize ADIs of various formats and exploit common VFL systems. We further launch greybox fuzz testing, guided by the resiliency score of “victim” participants, to perturb adversary-controlled inputs and systematically explore the VFL attack surface in a privacy-preserving manner. We conduct an in-depth study on the influence of critical parameters and settings in synthesizing ADIs. Our study reveals new VFL attack opportunities, promoting the identification of unknown threats before breaches and building more secure VFL systems.

1 INTRODUCTION

A traditional machine learning system workflow involves a data pipeline, which uses a central server that hosts the trained model to make predictions. Thus, all data collected by local devices and sensors are sent back to the central server for model training and making predictions. This data integration technique necessitates users sharing their data with a central server, which is strongly opposed due to a variety of real-world concerns, including data privacy, industrial competition, and complex administrative procedures.

To address this problem, collaborative learning, also known as federated learning [89], retains private data locally to train intermediate models. The parameters of these locally trained intermediate models are then aggregated into a single, consolidated, and gradually improved global model. Model aggregation uses either a trusted central coordinator or secure computation protocols like secure multi-party computation (MPC) [33]. Depending on how local data are distributed, federated learning systems can be classified into

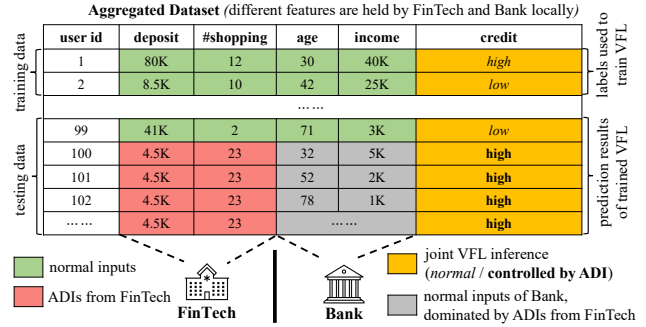


Figure 1: ADIs from FinTech dominate the VFL predictions.

vertical federated learning (VFL) [40, 89] and horizontal federated learning (HFL) [15, 61]. Unlike centralized machine learning, federated learning shares only parameters, not sensitive data, thus mitigating privacy leakage concerns.

Despite the significant development of federated learning for aggregating dispersed data across participants, emerging attacks targeting this new computing paradigm have been revealed. In particular, the distribution of the training process to a set of potentially malicious clients creates backdoor attack or adversarial example (AE) opportunities on the shared model [10, 14, 75, 80, 82, 87]. However, while practical attacks have been proposed toward HFL [10, 14, 87], attack vectors of VFL have not been systematically studied.

This research examines security issues of VFL in light of its growing adoption in security- and privacy-sensitive domains such credit scoring, insurance, and loan assessment [89]. Particularly, we find that a set of unique inputs, which we call *adversarial dominating inputs* (ADIs), can primarily influence and dominate the joint model predictions of multiple VFL participants in an unexpected manner. Fig. 1 presents the scenario that in vertical federated logistic regression (HeteroLR) task [40], one participant \mathcal{A} holds data from a FinTech, while participant \mathcal{B} holds data from a bank. They jointly predict a user’s credit level in a privacy-preserving manner, such that \mathcal{A} and \mathcal{B} cannot see each other’s data. Fig. 1 highlights the normal usage situation in green. However, we find that by perturbing \mathcal{A} ’s data into ADIs (red in Fig. 1), \mathcal{A} controls the joint prediction to a fixed answer at his will, and diminishes the influence of \mathcal{B} ’s data (grey in Fig. 1).

This research, as the first systematic study on ADIs in VFL, is motivated by findings in Fig. 1. We first formulate ADIs and prove their existence in common VFL protocols. Then, in two steps, we explore ADIs in real-world VFL systems. First, we design gradient-based approaches for ADI synthesis in both *whitebox* and *blackbox* settings. Second, inspired by feedback-driven software fuzzing, we design a *greybox* fuzz testing framework to uncover ADIs. The

proposed two-step approaches delineate attack vectors using ADIs from different perspectives and at varying costs: gradient-based methods demonstrate how attackers can initiate an end-to-end exploitation using ADIs by controlling a participant, whereas fuzz testing enables in-house vulnerability assessment to comprehensively uncover ADIs in a privacy-preserving manner under VFL participants’ collaboration.

Our evaluation includes three popular VFL systems with various input formats (e.g., images, table data). We achieve promising success rates of gradient-based ADI synthesis and illustrate the stealth of synthesized ADIs by comparing them with normal inputs. We also find 1,486 ADIs over 40 hours of fuzzing, revealing large attack surfaces of popular VFL systems. We investigate how several key parameters and settings can influence ADI synthesis and uncovering. Overall, we show that the ADI issue is a crucial but often neglected impediment in adopting VFL in real-world circumstances. In sum, this study makes the following contributions:

- We find a new attack vector in VFL, where certain inputs of adversary-controlled VFL participants, namely ADIs, can dominate the joint inference made by VFL. ADIs extensively diminish other participants’ contribution to model inference, thus hogging the rewards provided to incentivize VFL participants contributing important features.
- We prove the existence of ADIs in popular VFL systems. We propose gradient-based methods for ADI synthesis. We design a fuzzing tool to comprehensively uncover ADIs and facilitate vulnerability assessment of VFL systems. Our method is adaptable to various VFL systems and input formats.
- We achieve high success rates of generating ADIs to exploit VFL systems, indicating that ADIs are prevalent yet neglected issues. Our insights can provide users with the up-to-date understanding of VFL systems.

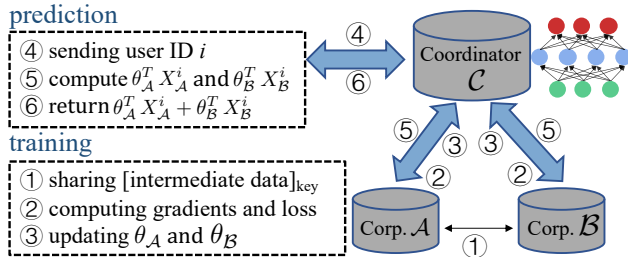


Figure 2: Architecture of a VFL system.

2 BACKGROUND

VFL Overview. In VFL, each participant learns from distinct feature partitions within a same data sample. Given two participants \mathcal{A} and \mathcal{B} , features X^i of a data sample i are partitioned into $X_{\mathcal{A}}^i$ and $X_{\mathcal{B}}^i$ ($X^i = X_{\mathcal{A}}^i || X_{\mathcal{B}}^i$; $||$ is the concatenation) and possessed separately by \mathcal{A} and \mathcal{B} . As shown in Fig. 1, a regional FinTech and a bank located in the same region maintain records of many local residents. To predict a resident i ’s credit score, the bank and the FinTech can extract his financial records and make the joint inference. Although data maintained by the FinTech and the bank have very different

feature spaces, they belong to the same user i . The prediction results will be aggregated in a coordinator \mathcal{C} (omitted in Fig. 1) and returned to \mathcal{A} and \mathcal{B} .

During training, VFL participants exchange intermediate information and compute training losses and gradients in a privacy-preserving manner, where raw data are kept locally by each participant. Fig. 2 depicts a typical VFL scenario, where two participants \mathcal{A} and \mathcal{B} jointly train a model. \mathcal{A} also possesses the corresponding labels to facilitate training. Some VFL systems would also require a coordinator \mathcal{C} . Holistically, model training can be divided into three steps: 1) \mathcal{A} and \mathcal{B} encrypt and exchange the intermediate stages for gradient and loss calculations; 2) \mathcal{A} and \mathcal{B} compute the encrypted gradients, and \mathcal{A} computes the encrypted loss and uploads the encrypted gradients and losses to \mathcal{C} ; and 3) \mathcal{C} decrypts the gradients and updates the models’ parameters $\theta_{\mathcal{A}}$ and $\theta_{\mathcal{B}}$, and then sends them back to \mathcal{A} and \mathcal{B} .

To use a trained VFL system, common user IDs $i \in I$ shared by \mathcal{A} and \mathcal{B} must be first confirmed [71]. The corresponding records will be extracted (④ in Fig. 2), and each participant will compute the local intermediate results which will be aggregated in \mathcal{C} (⑤ in Fig. 2). \mathcal{C} will compute the joint prediction result and return it to \mathcal{A} and \mathcal{B} (⑥ in Fig. 2).

VFL vs. HFL. Unlike HFL, where participants are normal users with data in the same domain, VFL participants are usually companies holding data in different domains. In HFL, all participants receive the same model from a central server, whereas in VFL, local models hold by participants are distinct and the central server coordinates with participants to make joint predictions. Also, we clarify that most VFL designs have 2 (maximum 4) participants in general [24, 57, 86, 89].

Learning Protocols. We introduce two popular VFL systems: vertical federated logistic regression (HeteroLR) [40] and vertical federated neural network (SplitNN) [39]. They are widely used in real-world VFL scenarios and show comparable performance with their centralized versions. More importantly, most parameter-based learning methods in VFL can be extended from these two core protocols. For instance, the vertical federated visual question answering (VFVQA), a popular paradigm facilitating answering questions about images [51], is extended from SplitNN. Hence, our proof on ADI existence (Sec. 3.3) and evaluation (Sec. 7) subsume SplitNN and HeteroLR. We also implement and evaluate VFVQA by extending SplitNN. We present the training and implementation details of all three protocols in Appendix A.

VFL Rewarding. VFL enables an individual participant (e.g., a bank) to enrich its data by incorporating data from other participants. Participants will be rewarded for their contributions to the joint inference as is standard in collaborative learning. Federated learning participants are often rewarded following a “pay-per-use” model [59, 73, 78, 91], where participants are compensated according to the *importance* of their contributed data in each joint prediction [56, 84].

3 PROBLEM STATEMENT

3.1 Related Work & Motivation

Distributed Machine Learning Systems. Advances in distributed machine learning systems have enabled large-scale machine learning algorithms to be run in a distributed manner [17, 23, 47, 67, 69, 81]. Horizontal collaborative learning, also known as horizontal federated learning, was developed to provide an efficient and privacy-preserving approach for distributed machine learning [61], in which clients only share model updates rather than training data. The concept of collaborative learning is expanded further into a vertical paradigm, namely VFL [40, 65, 89], in which clients hold separate features that belong to the same users.

Attacks on Collaborative Learning Systems. Existing research has shown that representative deep learning attacks, such as backdoor and training data reconstruction attacks, can be launched in collaborative learning settings. Nevertheless, most existing works either attack HFL [10, 14, 18, 27, 31, 64, 75, 77, 80, 82, 87], or attack VFL in a different way [52, 56, 83], e.g., inferring private data of victim participants. For instance, Bagdasaryan et al. [10] replaced the global model with a malicious local model by scaling up the attacker’s updates, thus enabling the modeling of backdoor attacks in one iteration of the model update. Bhagoji et al. [14] propose a model poisoning attack by controlling a few malicious agents, making the central model to misclassify chosen inputs. Xie et al. [87] exploit the distributed nature of federated learning by decomposing a backdoor trigger into several local patterns and embedding each into an adversarial client’s training set. A recent unpublished work [83] conducts private training data leakage attacks via deliberately-modified gradients. In contrast, this work aims to manipulate joint VFL inference using ADIs in a stealthy manner. Our novel attack enables an adversary to control VFL joint prediction towards his will, reduce others’ contribution, and hog rewards used to incentivize participants. These underlie the key novelty of our work.

Hardening Collaborative Learning Systems. Bonawitz et al. [16] introduce secure aggregation to defeat a semi-honest host and the dropout of arbitrary users. Pillutla et al. [68] propose a robust aggregation scheme toward corrupted client updates. FoolsGold mitigates sybil-based poisoning attacks based on the diversity of client updates [30]. Li et al. [48] enhance the fairness of resource allocation in HFL. Holistically, our present study assesses the unfair contribution of VFL participants and the security implications.

ADI vs. Standard AE. Methods generating standard AEs in centralized learning or HFL [9, 35] can also be extended to VFL systems. However, in VFL scenarios, AEs and ADIs differ in two aspects. First, ADIs only control a subset of features (e.g., in Fig. 1, only FinTech’s features are controlled), whereas AEs control the whole feature space. Second, ADIs aim to dominate practically all inputs from victim participants, while AEs usually misclassify a specific input to a targeted label. When the victim participant takes another input, the same AE is unlikely to mislead the prediction again. Also, in formulating the adversary’s objective, AEs do not consider victim participants’ contribution. In contrast, ADIs explicitly minimize the victim participants’ contribution, thus hogging rewards used to incentivize participants contributing important features.

3.2 Threat Model

Attack Scenario. This research considers m participants that jointly train a VFL model by consolidating their local datasets. We assume that the inputs of one participant are controlled by the adversary. We refer to this adversarial participant as \mathcal{A} , and the rest $m - 1$ benign participants as \mathcal{B}_j where $j \in \{1, \dots, m - 1\}$. We also refer to the central coordinator used by a VFL system as \mathcal{C} . The feature space X^i of a data sample i is thus partitioned into $X^i = X_{\mathcal{A}}^i || X_{\mathcal{B}_1}^i || \dots || X_{\mathcal{B}_{m-1}}^i$ and held by different participants.

Adversary’s Objectives. \mathcal{A} aims to dominate the joint inference using ADIs and extensively diminish the contribution of other participants. This way, \mathcal{A} can control the result towards the direction of his will and hog the vast majority of rewards, given that only \mathcal{A} contributes non-trivial features to the joint prediction. We formally define ADIs as following:

Definition 1 (ADIs). Consider VFL system with m participants, $f(X_{\mathcal{A}}, X_{\mathcal{B}_1}, \dots, X_{\mathcal{B}_{m-1}})$, an input $X_{\mathcal{A}}^*$ is regarded as an ADI when the output of the VFL system is not influenced by changing the inputs from participants \mathcal{B}_j , where $j \in \{1, \dots, m - 1\}$. Formally, we regard $X_{\mathcal{A}}^*$ as an ADI when the following holds:

$$\forall X_{\mathcal{B}} \in D_{\mathcal{B}} (f(X_{\mathcal{A}}^*, X_{\mathcal{B}_1}, \dots, X_{\mathcal{B}_{m-1}})) \leq \epsilon \quad (1)$$

, where small value ϵ is the dominating threshold and $X_{\mathcal{B}} \in D_{\mathcal{B}}$ is short for $X_{\mathcal{B}_1} \in D_{\mathcal{B}_1}, \dots, X_{\mathcal{B}_{m-1}} \in D_{\mathcal{B}_{m-1}}$.

Eq. 1 illustrates that $X_{\mathcal{A}}^*$ is regarded as an ADI when the variance of the output is bounded by ϵ w.r.t. the change of inputs from $\mathcal{B}_1, \dots, \mathcal{B}_{m-1}$. This way, \mathcal{A} dominates the joint prediction, no matter what inputs are used by participants $\mathcal{B}_1, \dots, \mathcal{B}_{m-1}$. Consider the VFL example in Fig. 1, where a bank and a FinTech jointly predict a user’s credit score. An adversarial FinTech can use ADIs to control the joint inference; for instance, the joint inference can be forced to always yield high credit scores, despite poor financial records (“income” in Fig. 1) the users may have in the bank.

Adversary’s Capability. We assume that the adversary \mathcal{A} can arbitrarily perturb its inputs to generate ADIs. We also assume that in the VFL joint prediction stage, all inputs of \mathcal{B} follow the distribution of their training dataset. To generate ADIs, we assume that a *tiny* sample dataset, serving as \mathcal{B} ’s normal inputs, is available to \mathcal{A} . We refer to this *tiny* sample dataset as \mathcal{S} . \mathcal{S} does not deviate from the distribution of \mathcal{B} ’s standard inputs. Nevertheless, \mathcal{S} is not necessarily from \mathcal{B} ’s training data. Given a well-trained VFL model, we assume that it is feasible for \mathcal{A} to collect the tiny dataset \mathcal{S} in the following ways. First, \mathcal{A} can conspire with a *small* group of users who behave normally when generating the data to form \mathcal{S} . These users submit \mathcal{S} to \mathcal{B} and also disclose \mathcal{S} to \mathcal{A} (see Sec. 4.2 for an end-to-end diagram of this strategy). Second, recent privacy inference attacks [56, 83] can also effectively infer data samples possessed by \mathcal{B} .

Indeed, our study shows that to generate ADIs that dominate at least 95% of inputs in \mathcal{B} (threshold “95%” is clarified in the last paragraph of Sec. 3.4), we only need a tiny \mathcal{S} whose elements are randomly selected from the test dataset of \mathcal{B} , which is never revealed to \mathcal{B} during training. Sec. 7 reports that we require only 20 MNIST images (i.e., about 0.03% of MNIST) to dominate 95% of inputs in its test dataset. We empirically study how $|\mathcal{S}|$ influences

Table 1: \mathcal{A} 's accessibility under different schemes.

	Whitebox ADI Synthesis	Blackbox ADI Synthesis	Greybox Fuzz Testing
\mathcal{B} 's model	✓	×	×
\mathcal{B} 's training dataset	×	×	×
majority of \mathcal{B} 's test dataset	×	×	×
tiny dataset \mathcal{S}^1	✓	✓	×
saliency score of \mathcal{B}	N/A	N/A	✓
Collaboration of all participants	×	×	✓
Computation cost	low	high	medium

¹ \mathcal{A} can collect the *tiny* dataset \mathcal{S} by either launching data inference attacks [56, 83] or conspiring with a few users, as clarified in threat model. In our implementation, \mathcal{S} is formed by taking a few samples from the test dataset of \mathcal{B} randomly.

the synthesis of ADIs in Sec. 7.4. We also discuss the selection of \mathcal{S} in Sec. 8.

Three Methods for ADI Synthesis or Uncovering. We consider whitebox and blackbox attacks to synthesize ADIs. In the whitebox setting, we assume that \mathcal{A} has access to the trained local model $M_{\mathcal{B}}$ on the victim participant \mathcal{B} . Hence, for each input $X_{\mathcal{B}}^i \in \mathcal{S}$, \mathcal{A} can acquire the corresponding gradients when $M_{\mathcal{B}}$ is processing $X_{\mathcal{B}}^i$. This is *consistently assumed* by previous VFL inference attacks [56], given that this information is essential for participants and coordinator \mathcal{C} to justify the effectiveness of the trained model and explain prediction results [89]. Moreover, Sec. 4.2 demonstrates attacks with *no* access to the trained model $M_{\mathcal{B}}$. For this blackbox setting, our encouraging findings show that attack success rates decrease only slightly; see the last paragraph of Sec. 7.1.

We also propose a fuzz testing framework to uncover ADIs (Sec. 5). Fuzzing helps VFL developers comprehensively detect ADIs and perform security assessment (which is hardly feasible for our gradient-based approach given the high cost and privacy consideration; see Table 1). For fuzzing, \mathcal{A} does not need to access \mathcal{S} . Instead, participants share a saliency score to guide fuzzing (comparable to how code coverage guides software fuzzing [93]). This saliency score is a floating number derived from the saliency map's L^1 norm. That is, to protect participants' data privacy, information of *low sensitivity* is shared instead of saliency maps.

We summarize assumptions in Table 1, where ✓ means that \mathcal{A} requires to access the corresponding model/data. We also compare three methods regarding the computation cost; blackbox attacks estimate gradients, thus imposing the highest computation cost. Greybox fuzzing is guided by saliency scores, whereas whitebox ADI synthesis denotes a more straightforward (and lightweight) generation process under objectives. We clarify details of each attack in Sec. 4 and Sec. 5. Readers may also refer to Appendix B for an end-to-end illustration of blackbox ADI synthesis.

3.3 Proof on the Existence of ADIs in VFL

This work proves that ADIs exist in two VFL systems: HeteroLR and SplitNN. As introduced in Sec. 2, most parameterized VFL systems can be extended from these two. Sec. 3.4 discusses the generalization. Below, we consider two participants and discuss extension to more participants in Sec. 3.4.

ADI in HeteroLR. Participant \mathcal{A} holds the data $X_{\mathcal{A}} \in D_{\mathcal{A}}$, whereas participant \mathcal{B} holds the data $X_{\mathcal{B}} \in D_{\mathcal{B}}$ following any distribution whose density function is $p(X_{\mathcal{B}})$. \mathcal{A} is controlled by an adversary, whereas \mathcal{B} behaves normally. $\theta_{\mathcal{A}}$ and $\theta_{\mathcal{B}}$ are their corresponding coefficients. The HeteroLR output can thus be expressed as:

$$f(X_{\mathcal{A}}, X_{\mathcal{B}}) = g(\theta_{\mathcal{A}}^T X_{\mathcal{A}} + \theta_{\mathcal{B}}^T X_{\mathcal{B}})$$

, where $g(t) = \frac{1}{1+e^{-t}}$ is the Sigmoid function, $X_{\mathcal{A}} \in \mathbb{R}^{d_1}$, $\theta_{\mathcal{A}} \in \mathbb{R}^{d_1}$, $X_{\mathcal{B}} \in \mathbb{R}^{d_2}$, and $\theta_{\mathcal{B}} \in \mathbb{R}^{d_2}$. d_1, d_2 denote dimensions of the features in \mathcal{A} and \mathcal{B} . We have the following corollary:

Corollary 1 (Variance of HeteroLR). *With fixed input $X_{\mathcal{A}}^*$ and varying input $X_{\mathcal{B}}$ following any distribution whose density function is $p(X_{\mathcal{B}})$, the output variance of HeteroLR is:*

$$\begin{aligned} & \mathbb{V}_{X_{\mathcal{B}} \in D_{\mathcal{B}}}(f(X_{\mathcal{A}}^*, X_{\mathcal{B}})) \\ &= \sum_{k=1}^{\mathcal{K}} \pi_k \Phi\left(\frac{\mu'_k}{\sqrt{\sigma_1^2 + \sigma_k'^2}}\right) \left(1 - \sum_{k=1}^{\mathcal{K}} \pi_k \Phi\left(\frac{\mu'_k}{\sqrt{\sigma_1^2 + \sigma_k'^2}}\right)\right) \\ &+ \sum_{k=1}^{\mathcal{K}} -\frac{\pi_k}{\sqrt{2\pi}} \frac{1}{\sqrt{\sigma_k'^2 + \sigma_2^2}} \exp\left\{-\frac{1}{2} \frac{\mu_k'^2}{\sigma_k'^2 + \sigma_2^2}\right\} \end{aligned}$$

, where the density function $p(X_{\mathcal{B}})$ is approximated by Gaussian Mixture Model: $p(X_{\mathcal{B}}) \approx \sum_{k=1}^{\mathcal{K}} \pi_k \mathcal{N}(X_{\mathcal{B}} | \mu_{\mathbf{k}}, \Sigma_{\mathbf{k}})$, $\sum_{k=1}^{\mathcal{K}} \pi_k = 1$, $\pi_k > 0$, \mathcal{K} is a finite number, $\mu_{\mathbf{k}} \in \mathbb{R}^{d_2}$, $\Sigma_{\mathbf{k}} \in \mathbb{R}^{d_2 \times d_2}$, $\mu'_k = \theta_{\mathcal{A}}^T X_{\mathcal{A}}^* + \theta_{\mathcal{B}}^T \mu_{\mathbf{k}}$, $\sigma_k'^2 = \theta_{\mathcal{B}}^T \Sigma_{\mathbf{k}} \theta_{\mathcal{B}}$, $\sigma_1 = 1.699$, and $\sigma_2 = 1.630$.

According to Corollary 1, with unbounded $X_{\mathcal{A}}^*$ and $\|\theta_{\mathcal{A}}\|_1 > 0$, the range of $\theta_{\mathcal{A}}^T X_{\mathcal{A}}$ is $(-\infty, +\infty)$. Thus, the variance of the output is bounded when $\theta_{\mathcal{A}}^T X_{\mathcal{A}} \rightarrow -\infty$: $\lim_{\theta_{\mathcal{A}}^T X_{\mathcal{A}} \rightarrow -\infty} \mathbb{V}_{X_{\mathcal{B}} \in D_{\mathcal{B}}}(f(X_{\mathcal{A}}^*, X_{\mathcal{B}})) = 0^+$. For any $\epsilon > 0$, there exists $X_{\mathcal{A}}^*$ satisfying $\mathbb{V}_{X_{\mathcal{B}} \in D_{\mathcal{B}}}(f(X_{\mathcal{A}}^*, X_{\mathcal{B}})) \leq \epsilon$. According to Definition 1, $X_{\mathcal{A}}^*$ is an ADI for HeteroLR. We prove Corollary 1 in Appendix C.

ADI in SplitNN. Similarly, in SplitNN, $X_{\mathcal{A}} \in D_{\mathcal{A}}$ and $X_{\mathcal{B}} \in D_{\mathcal{B}}$ are the corresponding local outputs from participants \mathcal{A} and \mathcal{B} , and the coordinator model is a single-layer fully connected network, with ReLU as its activation function. The output of SplitNN is:

$$f(X_{\mathcal{A}}, X_{\mathcal{B}}) = \text{ReLU}(w^T [X_{\mathcal{A}} || X_{\mathcal{B}}]) = \text{ReLU}(w_{\mathcal{A}}^T X_{\mathcal{A}} + w_{\mathcal{B}}^T X_{\mathcal{B}})$$

, where $||$ is concatenation and w denotes the parameter of the coordinator model. $X_{\mathcal{A}} \in \mathbb{R}^{d_1}$, $w_{\mathcal{A}} \in \mathbb{R}^{d_1}$, $X_{\mathcal{B}} \in \mathbb{R}^{d_2}$ and $w_{\mathcal{B}} \in \mathbb{R}^{d_2}$. d_1, d_2 are dimensions of the outputs in \mathcal{A} and \mathcal{B} . $X_{\mathcal{B}}$ follows any distribution whose density function is $p(X_{\mathcal{B}})$. We have the following corollary.

Corollary 2 (Variance of SplitNN). *With fixed input $X_{\mathcal{A}}^*$ and varying input $X_{\mathcal{B}}$ following any distribution whose density function is $p(X_{\mathcal{B}})$, the output variance of SplitNN is:*

$$\begin{aligned} & \mathbb{V}_{X_{\mathcal{B}} \in D_{\mathcal{B}}}(f(X_{\mathcal{A}}^*, X_{\mathcal{B}})) \\ &= \left(\sum_{k=1}^{\mathcal{K}} \pi_k \Phi\left(\frac{\mu'_k}{\sigma_k}\right)\right) \left(\sum_{k=1}^{\mathcal{K}} \pi_k^2 \sigma_k'^2 \left(1 - \frac{\mu'_k}{\sigma_k'} \frac{\phi\left(\frac{\mu'_k}{\sigma_k'}\right)}{\Phi\left(\frac{\mu'_k}{\sigma_k'}\right)} - \left(\frac{\phi\left(\frac{\mu'_k}{\sigma_k'}\right)}{\Phi\left(\frac{\mu'_k}{\sigma_k'}\right)}\right)^2\right)\right) \\ &+ \left(\sum_{k=1}^{\mathcal{K}} \pi_k \left(\mu'_k + \sigma_k' \frac{\phi\left(\frac{\mu'_k}{\sigma_k'}\right)}{\Phi\left(\frac{\mu'_k}{\sigma_k'}\right)}\right)\right)^2 \left(1 - \sum_{k=1}^{\mathcal{K}} \pi_k \Phi\left(\frac{\mu'_k}{\sigma_k'}\right)\right) \end{aligned}$$

, where the density function $p(X_{\mathcal{B}})$ is approximated by Gaussian Mixture Model: $p(X_{\mathcal{B}}) \approx \sum_{k=1}^{\mathcal{K}} \pi_k \mathcal{N}(X_{\mathcal{B}} | \mu_{\mathbf{k}}, \Sigma_{\mathbf{k}})$, $\sum_{k=1}^{\mathcal{K}} \pi_k = 1$, $\pi_k > 0$, \mathcal{K} is a finite number, $\mu'_k = w_{\mathcal{A}}^T X_{\mathcal{A}}^* + w_{\mathcal{B}}^T \mu_{\mathbf{k}}$, and $\sigma_k'^2 = w_{\mathcal{B}}^T \Sigma_{\mathbf{k}} w_{\mathcal{B}}$.

According to Corollary 2, with unbounded $X_{\mathcal{A}}^*$ and $\|w_{\mathcal{A}}\|_1 > 0$, the range of $w_{\mathcal{A}}^T X_{\mathcal{A}}$ is $(-\infty, +\infty)$. Thus, $\lim_{w_{\mathcal{A}}^T X_{\mathcal{A}} \rightarrow -\infty} \mu'_k = -\infty$ and $\lim_{w_{\mathcal{A}}^T X_{\mathcal{A}} \rightarrow -\infty} \mathbb{V}_{X_{\mathcal{B}} \in D_{\mathcal{B}}} (f(X_{\mathcal{A}}^*, X_{\mathcal{B}})) = 0^+$. For any $\epsilon > 0$, there must exist $X_{\mathcal{A}}^*$ satisfying $\mathbb{V}_{X_{\mathcal{B}} \in D_{\mathcal{B}}} (f(X_{\mathcal{A}}^*, X_{\mathcal{B}})) \leq \epsilon$. Thus, according to Definition 1, $X_{\mathcal{A}}^*$ is an ADI for this SplitNN protocol. We provide the detailed proof for Corollary 2 in Appendix D.

3.4 Extension & Practical Consideration

Generalization. Sec. 2 has clarified that most parameter-based VFL systems are extensions of HeteroLR and SplitNN. These models all concatenate features from the same data sample to form a joint inference. Thus, we assume that Corollary 1 and Corollary 2 subsume most real-world cases, illustrating the generalization of our attack. Our evaluation (Sec. 7) also attacks VFVQA, an extension of SplitNN. We also discuss attack tree-based VFL in Sec. 8.

Bounded Mutation. We have proved the existence of ADIs when arbitrarily mutating $X_{\mathcal{A}}^*$. Nevertheless, arbitrary mutation can generate unrealistic ADIs, which may not be desirable in real-world exploitations. We design a bounded mutation scheme to generate more realistic inputs. Bounded mutation perturbs $X_{\mathcal{A}}^*$ within a predefined range, e.g., perturbing $X_{\mathcal{A}}^*$ within its variance in the standard dataset. We also prove the existence of ADIs under bounded mutation in Appendix E. The generated ADIs are seen as indistinguishable from normal inputs, indicating a severe, practical, yet overlooked issue to VFL. We empirically evaluate the stealth of ADIs generated by bounded mutation in Sec. 7.1 and Sec. 7.2.

More Participants. As introduced in threat model (Sec. 3.2), we use ADIs to attack a VFL system of m participants, where m can be greater than two. While Corollary 1 and Corollary 2 are based on two participants \mathcal{A} and \mathcal{B} , our proofs can be easily extended to multi-participant VFL systems. To do so, features on $m - 1$ benign participants \mathcal{B} can be first aggregated into $X_{\mathcal{B}}$ to bridge with Corollary 1 and Corollary 2. Sec. 7.5 empirically assesses the presence of ADIs with various numbers of benign participants \mathcal{B} .

Practical Assessment of ADIs. Despite the inherent existence of ADIs in VFL, it is difficult, if at all possible, to obtain a complete view of \mathcal{B} 's inputs. Hence, we use the following practical assessment to decide if input $X_{\mathcal{A}}^*$ denotes an ADI:

Definition 2 (Practical Assessment of ADIs). *Consider VFL with m participants, $f(X_{\mathcal{A}}, X_{\mathcal{B}_1}, \dots, X_{\mathcal{B}_{m-1}})$, an input $X_{\mathcal{A}}^*$ is regarded as an ADI when the VFL joint prediction is not influenced by changing the inputs from participants \mathcal{B} . Formally:*

$$r(X_{\mathcal{A}}^*) = \frac{\sum_{i=1}^n \mathbb{I}(f(X_{\mathcal{A}}^*, X_{\mathcal{B}_1}^i, \dots, X_{\mathcal{B}_{m-1}}^i) = l_{target})}{n} \geq x\% \quad (2)$$

, where r computes the attack accuracy for $X_{\mathcal{A}}^*$, $x\%$ is the dominating threshold, n is the total number of samples in test dataset, and $\mathbb{I}(exp) = 1$, if exp is true, otherwise, $\mathbb{I}(exp) = 0$.

Our following study adopts this practical assessment, where an input of \mathcal{A} deems an ADI if the joint inference is confined as an attacker-specified label l_{target} for $x\%$ of the data samples in the standard input dataset of \mathcal{B} . x is empirically decided as 95 and 99, indicating that an ADI can extensively dominate 95% and 99% of the inputs from \mathcal{B} , respectively.

Algorithm 1 Gradient-Based ADI Synthesis.

```

1: function SALIENCY_EST( $X_{\mathcal{A}}^*, X_{\mathcal{B}}^i, M$ )
2:   output  $\leftarrow M(X_{\mathcal{A}}^*, X_{\mathcal{B}}^i)$ 
3:   saliency  $\leftarrow \|\frac{\partial Var(output)}{\partial X_{\mathcal{B}}^i}\|_1$ 
4:   return saliency
5: function ADI_GENERATION( $X_{\mathcal{A}}^*, M, l_{target}, Strategy, \mathcal{S}$ )
   $\triangleright r$ : computes attack accuracy as defined in Definition 2
   $\triangleright x\%, T$ : desired dominating threshold and maximum round
   $\triangleright \alpha, \beta, \gamma, \sigma$ : weight parameters
   $\triangleright \Lambda$ : feature-wise mutation constrain
   $\triangleright V, \delta_t$ : total mutation and mutation in round  $t$ 
   $\triangleright loss(X_{\mathcal{A}}^i, X_{\mathcal{B}}^i, M, l_{target})$ : loss between  $M(X_{\mathcal{A}}^i, X_{\mathcal{B}}^i)$  and  $l_{target}$ 
6:    $V \leftarrow 0, \delta_1 \leftarrow 0, t \leftarrow 1$ 
7:   while  $r(X_{\mathcal{A}}^*) \leq x\%$  and  $t \leq T$  do
8:     for each  $X_{\mathcal{B}}^i \in \mathcal{S}$  do
9:       if Strategy is RANDOM then
10:         $\delta_t \leftarrow \arg \min_{\delta_t} \alpha \text{Saliency\_est}(X_{\mathcal{A}}^* + V + \delta_t, X_{\mathcal{B}}^i, M)$ 
11:         $+ \beta \text{loss}(X_{\mathcal{A}}^* + V + \delta_t, X_{\mathcal{B}}^i, M, l_{target})$ 
12:       else
13:         $\delta_t \leftarrow \arg \min_{\delta_t} \alpha \text{Saliency\_est}(X_{\mathcal{A}}^* + V + \delta_t, X_{\mathcal{B}}^i, M)$ 
14:         $+ \beta \text{loss}(X_{\mathcal{A}}^* + V + \delta_t, X_{\mathcal{B}}^i, M, l_{target})$ 
15:         $+ \gamma \|\delta_t\|_2$  s.t.  $\|V + \delta_t\| \leq \Lambda$ 
16:         $\delta_t \leftarrow \sigma \delta_{t-1} + \delta_t, V \leftarrow V + \delta_t, t \leftarrow t + 1$ 
17:   return  $X_{\mathcal{A}}^* + V$ 

```

This section has formulated the research problem and presented discussions from various aspects. Sec. 4 describes gradient-based algorithms to synthesize ADIs. Sec. 5 proposes a fuzz testing-based approach to uncovering ADIs.

4 GRADIENT-BASED ADI SYNTHESIS

This section proposes a gradient-based ADI synthesis algorithm in line with our threat model in Sec. 3.2. Inputs of \mathcal{A} are mutated by the adversary, who aims to dominate the joint inference and minimize \mathcal{B} 's contribution. To assist ADI synthesis, \mathcal{A} can use dataset \mathcal{S} aligned with the distribution of \mathcal{B} 's normal inputs. In the whitebox setting, \mathcal{A} is able to access the trained models in \mathcal{B} and collect the gradients over samples in \mathcal{S} ; this ability is consistently assumed in prior VFL privacy inference attacks [56]. Sec. 4.2 discusses the extension to the blackbox setting.

Alg. 1 formulates ADI generation as an optimization problem. **ADI_GENERATION** is the main entry point of our algorithm, which takes the adversary-controlled input $X_{\mathcal{A}}^*$, jointly trained model M , adversary-targeted label l_{target} , the sample dataset \mathcal{S} , and a mutation strategy *Strategy* as the inputs. It returns the synthesized ADI $X_{\mathcal{A}}^* + V$, where V is the mutation vector over $X_{\mathcal{A}}^*$.

Random vs. Bounded Mutation. **ADI_GENERATION** requires to specify mutation strategies (i.e., random vs. bounded mutation) and proceed accordingly (lines 9–12). Given an input $X_{\mathcal{A}}^*$, random mutation perturbs $X_{\mathcal{A}}^*$ in all directions, whereas bounded mutation perturbs $X_{\mathcal{A}}^*$ within a predefined range. Bounded mutation is more conservative, such that the value of mutated $X_{\mathcal{A}}^*$ is confined within a reasonable range. Although defining a “reasonable” range for arbitrary $X_{\mathcal{A}}^*$ is challenging, we specify that mutations must be bounded by the variance of this feature in the training dataset.

Random mutation aims to minimize the output loss on a target label and the saliency contribution of inputs in \mathcal{S} (line 10 in Alg. 1; see below for the description of **SALIENCY_EST**). In contrast,

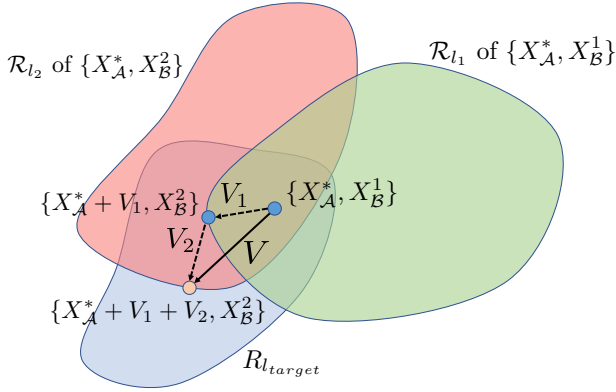


Figure 3: A schematic representation of the ADI generation algorithm over two participants \mathcal{A} and \mathcal{B} .

bounded mutation adds a penalty on the mutation to the objective (line 12). To facilitate a faster convergence, we use momentum (lines 13) to help accelerate updates in the right directions. Our evaluation, as will be reported in Table 4, empirically compares these two mutation strategies. As expected, random mutation manifests a higher chance of successfully generating ADIs, whereas bounded mutations induce more stealthy ADIs (see case studies in Sec. 7). **ADI GENERATION** supports both mutation schemes; users can select the one that best suits their needs.

Estimating Contributions of \mathcal{B} . **SALIENCEY_EST** computes the saliency score, denoting the contribution of X_B^i in a joint inference. We first calculate the derivative of the output’s variance for X_B^i , whose L^1 norm is further derived to estimate its saliency (line 3 in Alg. 1). A lower saliency score means that a modest change in X_B^i has minimal effect on the output, implying a negligible contribution of \mathcal{B} to the joint inference. This procedure aligns with the adversary’s objectives mentioned in Sec. 3.

4.1 A Schematic View of ADI Generation

Fig. 3 presents a schematic view to synthesize ADIs, where we proceed iteratively over a subset of \mathcal{B} ’s inputs and gradually generate ADIs as the input of \mathcal{A} . For a normal joint inference, both \mathcal{A} ’s and \mathcal{B} ’s inputs make non-trivial effects: when fixing \mathcal{B} ’s input as X_B^1 , perturbing X_A^* toward an ADI can form a high-dimensional classification region \mathcal{R}_{l_1} , where the joint inference over $\{X_A^*, X_B^1\}$ constantly yields l_1 . Similarly, input X_B^2 and X_A^* can form another region \mathcal{R}_{l_2} , whose induced inference is constantly l_2 .

Let \mathcal{S} be a dataset containing a non-trivial amount of \mathcal{B} ’s input samples, we assume the presumed existence of a special classification region $\mathcal{R}_{l_{target}}$. When $\{X_A^*, X_B^i\}$ where $X_B^i \in \mathcal{S}$ is inside its corresponding boundary \mathcal{R}_{l_i} and meanwhile inside $\mathcal{R}_{l_{target}}$, the joint inference yields label l_i . Nevertheless, when $\{X_A^*, X_B^i\}$ locates within $\mathcal{R}_{l_{target}}$ while outside any other regions $\mathcal{R}_{l_{other}}$, where $l_{other} \neq l_{target}$, the joint inference yields l_{target} . Thus, given $\{X_A^*, X_B^1\}$ locates inside \mathcal{R}_{l_1} in Fig. 3, perturbation V_1 sends the currently perturbed point, $\{X_A^* + V_1, X_B^1\}$, outside region \mathcal{R}_{l_1} and gets inside the region $\mathcal{R}_{l_{target}}$. When further dealing with X_B^2 paired with $X_A^* + V_1$, mutation V_2 sends the perturbed point, $\{X_A^* + V_1 + V_2, X_B^2\}$, outside region \mathcal{R}_{l_2} and gets inside the region

$\mathcal{R}_{l_{target}}$. By iterating \mathcal{S} and aggregating perturbation V_i into V , pairing $X_A^* + V$ with inputs in \mathcal{S} will be sent inside the region $\mathcal{R}_{l_{target}}$ but presumably outside of any other regions. We thus control the joint prediction when pairing $X_A^* + V$ with $X_B^i \in \mathcal{S}$. Moreover, Sec. 7.4 empirically shows that $X_A^* + V$ generated over \mathcal{S} achieves a high success rate of dominating at least 95% of \mathcal{B} ’s standard inputs. We deem $X_A^* + V$ as an ADI.

Compare with Universal AEs. Existing research has proposed methods in synthesizing universal adversarial examples (UAE) [62]. UAE launches a synthesis procedure similar to Fig. 3 and causes misclassification of many images using one unified perturbation. ADIs also result in a universal misclassification. To compare with UAE, we explicitly model and minimize victim participants’ contributions. Also, while most UAE techniques misclassify images into arbitrary labels [19, 62], we target a specified label l_{target} (see Fig. 3), and only allow perturbing adversary-controlled feature partition X_A^i instead of the entire feature space $X^i = X_A^i || X_{B_1}^i || \dots || X_{B_{m-1}}^i$. We also clarify that “universal” in UAE and ADIs have different meanings. UAE finds a universal perturbation to misclassify many images, whereas we find ADIs from a subspace of the entire feature space to *dominate all other subspaces possessed by victim participants*.

4.2 Extend To Blackbox ADI Synthesis

The machine learning community has proposed practical techniques to *estimate* gradients in a blackbox setting. Such methods have been commonly used in generating adversary examples [20, 44, 63, 79]. We thus present a gradient estimation-based approach to synthesizing ADIs; therefore, \mathcal{A} does not need to access the trained models on \mathcal{B} . We use the finite difference method (FDM) [37] to estimate the gradient in the following manner:

$$grad_B^k = \frac{Var(M(X_A^*, X_B^i + \delta_k)) - Var(M(X_A^*, X_B^i))}{\delta}$$

, where M is the joint model, X_A^* and X_B^i are the inputs fed to \mathcal{A} and \mathcal{B} . δ denotes a small perturbation and δ_k has the same dimension with X_B^i , whose k^{th} dimension is δ and the other dimensions are all 0. Every k^{th} dimension of input X_B^i has an estimated gradient $grad_B^k$, which can be aggregated to approximate the saliency gradient in Alg. 1 (line 3). With other parts remain the same in Alg. 1, we can thus synthesize ADIs in the blackbox setting.

Clarification. We clarify that conventional black-box AE attacks denote an *online* setting [38, 44, 76], where they require attackers to iteratively query a remote model (e.g., a cloud service) with recently mutated inputs and decide further mutations with estimated gradients. In contrast, for blackbox ADI synthesis, \mathcal{A} needs to acquire the joint inference results only over $X_B^i \in \mathcal{S}$ and $X_B^i + \delta_k \in \mathcal{S}^*$. \mathcal{A} pre-computes \mathcal{S} and \mathcal{S}^* *offline*, and as clarified in Sec. 3.2, \mathcal{A} then conspires with a small group of users, who submit \mathcal{S} and \mathcal{S}^* to \mathcal{B} . Therefore, we do not require the VFL to serve as a “cloud service” that actively processes unseen data (which is impractical in VFL scenarios). All data samples in \mathcal{S} and \mathcal{S}^* are computed *offline* and submitted to \mathcal{B} , before synthesizing ADIs. In short, our blackbox attack procedure is faithfully aligned with how VFL is used in real-life scenarios; see Appendix B for an end-to-end illustration of blackbox attack with diagrams.

5 UNCOVER ADIS WITH GREYBOX FUZZING

5.1 Motivation of Greybox Fuzz Testing

We clarify that excellent research has been done on testing distributed systems [11, 55, 92]; these works primarily focus on concurrency bugs. Contrarily, we launch privacy-preserving testing in the context of collaborative learning to uncover ADIs. The gradient-based ADI synthesis algorithm described in Sec. 4 can also be used to uncover ADIs. However, in-house quality assurance and vulnerability assessment are difficult, whose main reasons are twofold.

First, while malicious participant \mathcal{A} can synthesize ADIs without accessing the model of \mathcal{B} in blackbox ADI synthesis (see Sec. 4.2), the computation and communication overhead is substantial, especially when the feature dimension in \mathcal{B} is large. This is affordable for a malicious participant since **one ADI** is enough to manipulate nearly all joint predictions. However, gradient-based approaches are expensive for VFL users or developers who plan to **comprehensively collect ADIs for vulnerability assessment**.

Second, in the gradient-based algorithm, the malicious participant needs to prepare a small dataset \mathcal{S} . As clarified in Sec. 3.2 and Sec. 4.2, \mathcal{S} can be prepared by conspiring with a few users to submit \mathcal{S} to \mathcal{B} , or launching data inference attacks toward \mathcal{B} [56, 83]. However, for ethical users and developers, \mathcal{S} cannot be collected in the same way, as sharing user data may compromise privacy even if \mathcal{S} is minimal.

This section designs greybox fuzz testing to uncover ADIs without \mathcal{S} but under the collaboration with \mathcal{B} for in-house security assessment. Many studies have examined the use of (fuzz) testing to find inputs that can manipulate DNN model predictions [66, 88]. Nonetheless, we investigate a fresh design point — *efficient and privacy-preserving fuzz testing in VFL scenarios*.

5.2 Design of Greybox Fuzz Testing

Greybox software fuzzing is an evolutionary process in which inputs that reveal new code coverage are retained for more mutations until vulnerabilities are detected. In VFL, we consider an input $X_{\mathcal{A}}^*$ of participant \mathcal{A} interesting if $X_{\mathcal{A}}^*$ reduces contribution of other participants to the joint prediction. Although the “contribution” can be revealed using the saliency score, VFL systems do not allow such disclosure.

Inspired by our gradient-based ADI synthesis approach (Sec. 4), we extend the standard VFL systems by allowing participants to compute and share saliency scores to guide greybox fuzzing; the shared saliency score serves the feedback for fuzzing, which is comparable to how code coverage is used to guide software fuzzing [93]. We assume that:

Although sharing saliency may raise potential concerns of privacy violation, to assess ADI attack vectors before security breaches, normal participants should have enough incentive to collaborate and share the saliency scores.

Again, this stage allows VFL developers to launch **in-house vulnerability assessment by comprehensively uncovering ADIs**. The saliency score is derived from the the saliency map’s L^1 norm, which has *limited sensitivity*. Privacy leakage due to saliency score, though theoretically possible, is low in practice. Also, with more than 2 participants, several secure aggregation approaches can be

Algorithm 2 Saliency-Guided Greybox Fuzz Testing.

```

1: function IsADI( $X_{\mathcal{A}}^*, \mathcal{S}, l_{target}, M$ )
2:    $\mathcal{T} \leftarrow \emptyset$ 
3:   for each  $X_{\mathcal{B}}^i$  in  $\mathcal{S}$  do
4:      $o \leftarrow M(X_{\mathcal{A}}^*, X_{\mathcal{B}}^i)$ 
5:     add  $o$  in  $\mathcal{T}$ 
6:   return STABLE( $\mathcal{T}, l_{target}$ )
7: function FUZZING(Corpus of Seed Inputs  $\mathcal{C}, M, \mathcal{S}$ )
8:    $\mathcal{Q} \leftarrow \mathcal{C}, \mathcal{O} \leftarrow \emptyset$ 
9:   for 1 ... MAX_ITER do
10:    ( $X_{\mathcal{A}}^*, l_{target}$ )  $\leftarrow$  CHOOSENEXT( $\mathcal{Q}$ )
11:     $p \leftarrow$  ASSIGNENERGY( $X_{\mathcal{A}}^*$ )
12:    for 1 ...  $p$  do
13:       $X_{\mathcal{A}}^* \leftarrow$  MUTATE( $X_{\mathcal{A}}^*, \mathcal{S}, l_{target}, M$ )
14:      if IsADI( $X_{\mathcal{A}}^*, \mathcal{S}, l_{target}, M$ ) == true then
15:        add ( $X_{\mathcal{A}}^*, l_{target}$ ) in  $\mathcal{O}$ 
16:      else if REDUCESALIENCY( $X_{\mathcal{A}}^*, l_{target}, M$ ) == true then
17:        add ( $X_{\mathcal{A}}^*, l_{target}$ ) in  $\mathcal{Q}$ 
18:   return ADI Set  $\mathcal{O}$ 

```

used to shield each participant’s saliency score and increase privacy [13, 16].

Alg. 2 depicts the high-level procedure of our feedback-driven fuzzing. We clarify full implementation details of cooperating fuzzing with VFL in Appendix F. **FUZZING** is the entry point, where **IsADI** checks whether a given input $X_{\mathcal{A}}^*$ of \mathcal{A} can dominate other participants \mathcal{B} ’s contributions. **IsADI** allocates a set to collect all joint inference outputs (line 2). It then iterates all inputs $X_{\mathcal{B}}^i \in \mathcal{S}$ used by \mathcal{B} and records each joint inference output o (lines 4–5). **STABLE** checks whether outputs in \mathcal{T} are identical to its target label l_{target} .

FUZZING accepts a corpus of seeds \mathcal{C} to initialize queue \mathcal{Q} (line 8). This function also takes in the jointly trained model M and \mathcal{S} . For fuzzing, inputs in \mathcal{S} are *hidden* from \mathcal{A} . Rather, \mathcal{B} uses inputs in \mathcal{S} to cooperate with \mathcal{A} and facilitate **IsADI** and **MUTATE** (line 13 in Alg. 2). We use \mathcal{O} to store identified ADIs (line 8). The entire campaign is subjected to **MAX_ITER** iterations, and for each iteration, we pick one input $X_{\mathcal{A}}^*$ and its target label l_{target} by popping \mathcal{Q} (line 10) and determine #mutation over $X_{\mathcal{A}}^*$ (line 11). **MAX_ITER** is currently 5,000, and each $X_{\mathcal{A}}^*$ has a fixed “energy” of 20.

During each iteration, we generate a new variant $X_{\mathcal{A}}^*$ by mutating the original $X_{\mathcal{A}}^*$ (line 13). When ADIs are found (line 14), we add the input $X_{\mathcal{A}}^*$ into \mathcal{O} . In addition, $X_{\mathcal{A}}^*$ is “interesting” by successfully reducing the saliency of \mathcal{B} ; we thus add $X_{\mathcal{A}}^*$ to the queue for further mutations (lines 16–17). Alg. 2 will return all uncovered ADIs for users to assess security and attack interface of their VFL systems (line 18).

Design REDUCESALIENCY (Line 16). We decide whether input $X_{\mathcal{A}}^*$ of \mathcal{A} is prone to becoming an ADI by assessing its influence on \mathcal{B} , which can be modeled using the saliency scores of \mathcal{B} . As previously discussed, we assume that the saliency score is faithfully shared by \mathcal{B} . Software greybox fuzzing tools [93] look for inputs that achieve new code coverage. Similarly, **REDUCESALIENCY** checks whether $X_{\mathcal{A}}^*$ can successfully *decrease* the saliency scores shared by \mathcal{B} . This way, we identify and retain $X_{\mathcal{A}}^*$ to gradually minimize the contribution of \mathcal{B} . Note that saliency scores are computed using **SALIENCY_EST** presented in Alg. 1. Each saliency score, a floating number ranging from 0 to 1, is derived from the saliency map’s L^1 norm. A lower saliency score implies that \mathcal{B} contributes less to joint inference. The saliency score is more coarse-grained than the saliency map. It might not be inaccurate to assume that saliency

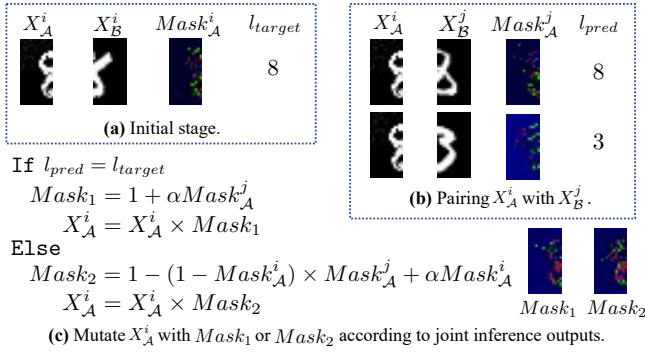


Figure 4: Saliency-aware mutation.

scores disclose only limited information regarding inputs of \mathcal{B} , pragmatically alleviating privacy leakage concerns.

Saliency-Aware Mutation (Line 13). We propose a saliency-aware scheme to mutate inputs. Fig. 4 illustrates the high-level procedure of this scheme using images from MNIST as an example. As will be introduced in Sec. 7, each MNIST image is vertically partitioned into two pieces in a VFL setting. Given a pair of input X_A^i and X_B^i belonging to the same MNIST image i , we first compute the saliency map of X_A^i as $Mask_A^i$ and the jointly inferred label l_{target} (Fig. 4(a)).

We mutate X_A^i with some random noise, and then iterate inputs in \mathcal{S} . For an input pair X_A^i and X_B^j ($j \neq i$), we compute a new saliency map $Mask_A^j$ (Fig. 4(b)). When the joint inference l_{pred} equals l_{target} , we retain this mutation by augmenting X_A^i with $\alpha Mask_A^j$ (If branch in Fig. 4(c)). $l_{pred} \neq l_{target}$ denotes undesirable mutations (Else branch in Fig. 4(c)); we weaken certain pixels in X_A^i in case they are focused by $Mask_A^j$ but overlooked by $Mask_A^i$. α is empirically decided as 0.2. $Mask_A^{i,j}$ is calculated using the algorithm in [29], where the saliency mask is a matrix with values ranging from 0 to 1. To boost a participant p 's contribution, according to [29], we can increase certain input components of p that correlate to large values on p 's saliency mask.

We repeat this procedure over inputs in \mathcal{S} to update X_A^i . We use *bounded mutation* over X_A^i to retain stealthy changes. The proposed mutation has a time complexity linear to $|\mathcal{S}|$. As $|\mathcal{S}|$ is tiny (e.g., 20 for our evaluation in Sec. 7.2), time complexity is not a major issue. Furthermore, our saliency-aware mutation is a general pipeline agnostic to input formats; it performs more holistic and efficient mutations than pixel-level mutations. Sec. 7.2 shows that a large number of ADIs are uncovered across all datasets using fuzz testing.

6 IMPLEMENTATION & EVALUATION SETUP

Our artifact contains around 8 KLOC, which includes codebase for attack and fuzz testing, as well as extensions of VFL frameworks. Our attack/fuzzing codebase can be integrated into different architectures of VFL systems. We train and test VFL models on Pytorch (ver. 1.8.0).

VFL Protocols & VFL Frameworks. As we discussed in Sec. 2, HeteroLR and SplitNN are two popular and core VFL protocols that can be extended to most parameterized VFL protocols (e.g., VFVQA). Hence, we evaluated these two protocols. To implement VFVQA, we

modify the state-of-the-art VQA model Oscar [49] into the VFL paradigm. In VQA, one participant raises natural-language questions about images possessed by the other participant. VFVQA allows two participants to conduct VQA while keeping questions/images locally; see Appendix A for VFVQA architecture and implementation details. To date, several federated learning infrastructures have been developed, including FATE [7], TF Federated [4], FedML [41], PySyft [3], and CrypTen [2]. We choose FATE and FedML due to their popularity and support for common VFL protocols including HeteroLR and SplitNN. FATE is maintained by a software enterprise, whereas FedML is a state-of-the-art VFL framework jointly developed by the research community and industry. Both platforms exhibit high engineering quality. Our main findings are, to our knowledge, independent to the underlying VFL frameworks. We use the default SplitNN implementation in FATE, and extend the HeteroLR implementation in FedML.

7 EVALUATION

Datasets & Environment Setup. We use five popular datasets: NUS-WIDE [22], Credit [1], Vehicle [5], MNIST [45], and VQA v2.0 [50]. Each dataset's features are partitioned between two VFL participants \mathcal{A} and \mathcal{B} , as shown in Table 2. For NUS-WIDE, \mathcal{A} holds the image features whereas \mathcal{B} holds the text features. For Credit, \mathcal{A} holds 13 features and \mathcal{B} holds 10. For Vehicle, both \mathcal{A} and \mathcal{B} get nine features. For MNIST, each image is vertically partitioned into two: \mathcal{A} gets the left piece (with 28×14 pixels) and \mathcal{B} gets the right. For VQA v2.0, \mathcal{A} holds images and \mathcal{B} raises natural-language questions. We summarize the detailed setup in Table 2. Please refer to the full details of dataset preparation and setup in Appendix G. Our evaluation is conducted on Intel Xeon CPU E5-2683 with 256 GB RAM and one Nvidia GeForce RTX 2080 GPU.

Success Rate. We measure the performance of our attack using success rates. Recall as we defined in Definition 2, to decide if an input X_A^i is ADI, we check if X_A^i can dominate more than a threshold of all test inputs of \mathcal{B} . As defined in Sec. 3, we adopt two thresholds (95% and 99%) as a practical assessment of ADIs. Accordingly, we define the ratio of samples from \mathcal{A} 's test dataset that can be successfully perturbed into ADIs as the attack "success rate" of ADI synthesis.

Dominating Inputs in Standard Datasets. Before synthesizing ADIs, we first assess the input dominating issues (without perturbation) in the standard datasets of \mathcal{A} . Using the aforementioned feature partition scheme, we train VFL models for two participants \mathcal{A} and \mathcal{B} . Table 3's last column shows that each trained model has achieved satisfying learning accuracy. Table 3 reports the dominating rates, i.e. the ratio of standard inputs of \mathcal{A} as ADIs. Recall when deciding if an input is ADI, our practical assessment (Definition 2) examines two thresholds, 95%, and 99%. The outlier is VQA v2.0, where an image is regarded as an ADI only when it dominates *all* of its associated questions (typically one image associated with 3–10 questions). Hence, the threshold should be 100.0% rather than 95% or 99% when assessing its input dominating issues. To ease the presentation, for Table 3 and the rest tables, we put the VQA v2.0 evaluation results in the 99% column and "NA" in the 95% column.

Credit has a greater dominating rate than other tasks under 95%. Credit is a binary classification task with a small sample size. Thus,

Table 2: Evaluation setup over VFL participants \mathcal{A} and \mathcal{B} .

Dataset	#Cases	Learning Protocol	Participant \mathcal{A}		Participant \mathcal{B}		Central Coordinator \mathcal{C}
			#Partitioned Features	Setup	#Partitioned Features	Setup	
NUS-WIDE	269,648	SplitNN	634	2-FCs with ReLU	1,000	2-FCs with ReLU	2-FCs with ReLU
Credit	30,000	HeteroLR	13	1-FC	10	1-FC	Sigmoid
Vehicle	946	HeteroLR	9	1-FC	9	1-FC	Sigmoid
MNIST	60,000	SplitNN	28×14 pixels	3-Convs with ReLU	28×14 pixels	3-Convs with ReLU	1-FC with ReLU
VQA v2.0	82,783	VFVQA	embedding to 50×2054	FasterRCNN [70]	embedding to 128×512	BERT [49]	Multi-Layer Transformers

Table 3: Dominating rates of the standard datasets.

	Dominating Rate		Model Accuracy on Test Datasets
	95%	99%	
NUS-WIDE	0.00%	0.00%	87.35%
Credit	25.0%	2.10%	0.7450 (auc-roc)
Vehicle	0.86%	0.14%	84.00%
MNIST	0.87%	0.20%	97.78%
VQA v2.0	NA	0.80%	73.82%

Table 4: Success rates of gradient-based ADI synthesis.

	Random Mutation		Bounded Mutation	
	95%	99%	95%	99%
NUS-WIDE	65.1%	49.6%	42.8%	22.0%
Credit	99.8%	99.6%	87.6%	52.6%
Vehicle	98.4%	97.0%	87.9%	74.8%
MNIST	92.9%	62.5%	34.5%	16.7%
VQA v2.0	NA	17.4%	NA	9.78%

it is likely to identify “dominating inputs” (i.e., false positives) of \mathcal{A} which induce identical classification outputs when paired with inputs of \mathcal{B} . To eliminate likely false positives, saliency maps of \mathcal{B} ’s inputs can be used to confirm if its contribution is negligible. Nevertheless, its dominating rate drops a lot under 99%. Overall, we interpret that dominating inputs are rare in well-designed and trained models with a fair feature partition. Without an active adversary, users are unlikely to notice ADIs until a security breach. Nevertheless, when feature partition over two participants is unbalanced, ADIs become noticeable; see Sec. 7.3.

7.1 Gradient-Based ADI Synthesis

Table 4 reports the success rate of ADI synthesis under different settings, thresholds, and mutation strategies. Complex datasets and models like NUS-WIDE, MNIST, and VQA v2.0 have a lower success rate than simple datasets like Credit and Vehicle, especially when the threshold is 99%. For Credit and Vehicle, the success rate is close to 100% under random mutation. Recall \mathcal{S} contains only 20 inputs of \mathcal{B} . Higher success rates can be achieved with more inputs in \mathcal{S} , as shown in Sec. 7.4. The bounded mutation scheme confines the applied mutations to a practical range (i.e., bounded by the variance of the mutated feature). We find that this scheme still achieves plausible success rates of over 50% for simple tasks like Credit and Vehicle and over 35% for complex tasks under the 95% threshold. 99% threshold is more challenging, and therefore, the success rate becomes reasonably lower. Overall, this evaluation shows that ADIs can be synthesized successfully despite variances in the evaluated datasets, VFL protocols, and mutation strategies. We envision that typical VFL systems can face high risks of being controlled by ADIs.

Stealth of ADIs. ADIs generated by bounded mutation mostly follow the distribution of the original datasets, making them visually similar to normal inputs. In Fig. 5, we project original inputs and ADIs synthesized under threshold 99% to 2D figures using multidimensional scaling. We interpret that ADIs generated by bounded mutation (marked in red) can neither be easily distinguished by the

data distribution nor by the distances between the data points. Fig. 6 reports stealthy ADIs synthesized by bounded mutation. While perturbing the left half of MNIST images (the first column of Fig. 6) only causes stealthy changes (the second column of Fig. 6), the synthesized ADIs, after concatenating with the right half of arbitrary MNIST images (i.e., the inputs of \mathcal{B} ; see the third column of Fig. 6), control the outputs to fixed labels (the last column of Fig. 6).

Fig. 7 shows some intriguing cases from the MNIST dataset. As shown in the “Concatenation/Expectation” column of Fig. 7, while ADIs may form reasonable digits (from a human perspective) with the inputs of \mathcal{B} , the joint inferences are still forced to be the target labels specified by the adversary. We also provide the saliency maps associated with the input images, which imply that the contribution of \mathcal{B} is negligible (the saliency maps in the 4th column barely have highlighted areas). This again shows that ADIs can govern the joint inference and negate other participants’ contributions.

We also clarify that whether concatenating ADIs and normal inputs can form meaningful contents largely depend on the nature of features that VFL participants hold. For instance, in MNIST, the features hold by different participants are images. Therefore, forming “meaningful concatenations” requires that both adversarial and benign participants provide *visually-correlated* images. This is apparently a challenging task, though a considerable number of successful cases (as in Fig. 7) are found in our evaluation. In contrast, datasets like Credit consist of low-dimensional numeric vectors; “visual correlation” is not a concern for such numeric data. It is generally easier for concatenations of ADIs and benign participant’s inputs to be in-distinguishable with normal data in Credit. In sum, though it is not the primary focus of this research, we deem it an interesting direction to explore synthesizing ADIs that can form meaningful concatenations with benign participants’ inputs. The challenge is that it is hard for the (adversarial-controlled) participant to quantify the distinguishability between the concatenations and normal inputs, and accordingly define an objective function.

Extend To Blackbox ADI Synthesis. Sec. 4.2 discusses estimating gradients with the finite difference method. We tested this strategy’s attack success rate using MNIST. The attack success rates using random mutation are 78.8% and 51.9% w.r.t. the 95% and 99% thresholds, respectively. Similarly, the results using bounded mutation are 33.9% and 4.85% w.r.t. the 95% and 99% thresholds. Compared with whitebox attacks (Table 4), the average success rates decrease only slightly. We present ADIs synthesized in the blackbox setting in Appendix H.

Reward Estimation under ADIs. Sec. 2 has discussed that federated learning clients are often compensated based on their contributions to the joint prediction. While the evaluated VFL frameworks do not ship with a reward calculation module, we estimate how ADIs influence reward allocation in Appendix I. As expected, while \mathcal{A} and \mathcal{B} earn roughly the same reward when using normal inputs,

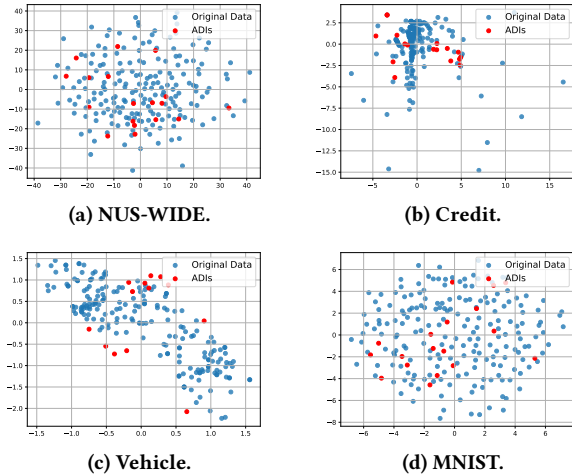


Figure 5: Normal inputs and ADIs projected to 2D figures.

\mathcal{A} 's Input Images Before/After Mutation	Three Images Input in \mathcal{B}	Fixed Joint Infer. Results
		8
		3
		7
		2

Figure 6: ADIs found in MNIST using bounded mutation.

ADI From \mathcal{A} / Normal Inputs From \mathcal{B}	Concatenation / Expectation	Fixed Joint Infer. Results
		2
		6
		6
		0

Figure 7: ADIs dominating the joint inference even when the concatenated images form reasonable digits.

ADIs allow adversary \mathcal{A} to hog rewards for each inference. We deem this evaluation as convincing to show that ADIs can create real-world financial loss and confusion for normal consumers.

7.2 Greybox Fuzz Testing

Fuzz testing helps in-house VFL vulnerability assessment. As mentioned in Sec. 5.2, we use bounded mutation to mutate inputs: bounded mutation generates more realistic inputs, which practically assesses VFL in front of stealthy ADIs.

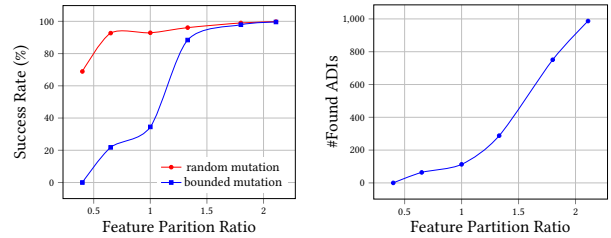
Table 5 reports the fuzzing results. For datasets with narrow feature spaces (Credit and Vehicle), we use 500 seeds and finish in two hours. For more complex datasets, we run a 12-hour campaign with a corpus of 1,000 seeds to systematically explore the input

Table 5: Fuzz testing results.

	#ADIs		#Seeds in Corpus	Processing Time
	95%	99%		
NUS-WIDE	176	98	1,000	12 hours
Credit	235	136	500	2 hours
Vehicle	392	157	500	2 hours
MNIST	113	86	1,000	12 hours
VQA v2.0	NA	93	1,000	12 hours

Table 6: Dominating rates of the standard dataset under different feature partition ratios.

Feature Partition Ratio	Dominating Rate on \mathcal{A}	Dominating Rate on \mathcal{B}	Model Accuracy on Test Datasets
0.40	0.00%	94.30%	97.55%
0.65	0.00%	20.49%	97.81%
1.00	0.87%	0.43%	97.78%
1.33	5.79%	0.00%	98.01%
1.80	50.40%	0.00%	98.20%
2.11	72.40%	0.00%	97.62%



(a) Gradient-based synthesis.

(b) Fuzz testing.

Figure 8: Performance under different feature ratios.

spaces. ADIs are found in similar numbers for all settings, indicating high efficiency of the proposed technique across input formats and VFL protocols. Recall that the fuzzing algorithm has relatively high time complexity; our saliency-aware mutation (line 13 in Alg. 2) and *IsADI* function (line 1 in Alg. 2) both require iterating all inputs in \mathcal{S} for each fuzzing iteration. Nevertheless, our results in Table 5 show that a high number of ADIs can be found in a half-day even for image inputs like VQA v2.0 and MNIST. We interpret the overall performance as plausible: the proposed approach allows developers to quickly assess the ADI risk of their VFL systems at a low cost.

Stealth of ADIs. We compare ADIs with normal inputs following the same procedure of reporting Fig. 5; the results are in Appendix H. We find that ADIs are highly similar to regular inputs. We also present several ADIs found by fuzzing and their saliency maps in Appendix H. Findings (i.e., ADIs greatly reduce the contribution of normal inputs) are consistent with Fig. 7.

7.3 Exploring Feature Partition Ratios

Recall in a typical VFL setting where each user ID i has a number of features X , each participant possesses a subset of features. This section studies how the success rate of ADI generation is affected by the feature partition ratio using MNIST. We re-run experiments in Table 3 to compare the dominating rates of standard datasets under various feature partition ratios (“feature” is the number of vertical dimensions of an MNIST image). Table 6 reports the findings: a feature partition ratio x denotes that \mathcal{A} possesses $x/(1+x)$ percent of the features in each data sample while \mathcal{B} has the rest. To be fair, we initialize all hyperparameters to the same value as Table 3. The model accuracies on the test dataset are all sufficiently high, indicating that models are well-trained.

Higher ratios imply that \mathcal{A} holds more features. Table 6 reports that when more features are allocated to a participant, more ADIs can likely be found on its side and dominate other participants. For instance, when the ratio reaches 2.11 (i.e., \mathcal{A} holds 19 columns while \mathcal{B} holds 9 columns of the image), the dominating rate is 72.40%, indicating that even without perturbation, 72.40% of \mathcal{A} 's normal inputs can control the joint inference. When the ratio falls below 0.65 (\mathcal{A} holds less than 8 columns), none of the original data samples in \mathcal{A} can control the joint inference, whereas data samples in \mathcal{B} dominate \mathcal{A} . When data samples are partitioned evenly (each participant gets 14 columns), the dominating rates on both sides are lower than 1%. In sum, we view this evaluation reveals a critical yet overlooked observation that in VFL, *numbers of features allocated on each participant should not largely deviate from each other; by contributing a comparable amount of "knowledge" to the joint inference, the trained model is seen to be more robust to ADIs*. Unbalanced feature partitioning causes concerns of dominating inputs and attackability.

Fig. 8a reports the success rate of ADI synthesis using different feature partitions. Consistent with Table 6, \mathcal{A} with more features can achieve greater success rates. The success rate is near 100% when the feature partition ratio surpasses 1.8. Fig. 8b explores how feature partitioning influences fuzzing. The fuzz testing, consistent with Sec. 7.2, starts with a corpus of 1,000 seeds. We run a 12-hour fuzzing campaign for each feature partition ratio. We find that when assigning \mathcal{A} with more features, fuzzing can uncover more ADIs.

VFL faces serious ADI issues when feature partitioning is largely unbalanced. To understand the root cause, assuming \mathcal{A} and \mathcal{B} hold feature partition dimensions d_1 and d_2 as their inputs where d_1 is notably larger than d_2 . The mutation V_{d_1} and V_{d_2} are performed on inputs of \mathcal{A} and \mathcal{B} , respectively. The parameters of \mathcal{A} and \mathcal{B} are $\theta_{\mathcal{A}d_1}$ and $\theta_{\mathcal{B}d_2}$. According to our observation, for \mathcal{A} holding d_1 and \mathcal{B} holding d_2 dimension of features, their parameters are roughly the same order of magnitude, meaning that $\frac{\|\theta_{\mathcal{A}d_1}\|_2}{d_1} \approx \frac{\|\theta_{\mathcal{B}d_2}\|_2}{d_2}$. Thus, the upper bound of $\|\theta_{\mathcal{A}d_1}^T V_{d_1}\|_1$ is: $\|\theta_{\mathcal{A}d_1}^T V_{d_1}\|_1 \leq \|V_{d_1}\|_2 \times \|\theta_{\mathcal{A}d_1}\|_2$. Similarly, $\|\theta_{\mathcal{B}d_2}^T V_{d_2}\|_1 \leq \|V_{d_2}\|_2 \times \|\theta_{\mathcal{B}d_2}\|_2$. With $\|V_{d_1}\|_2 = \|V_{d_2}\|_2$, and given d_1 is notably larger than d_2 , we have $\|\theta_{\mathcal{A}d_1}\|_2 > \|\theta_{\mathcal{B}d_2}\|_2$. Thus, the upper bound of $\|\theta_{\mathcal{A}d_1}^T V_{d_1}\|_1$ becomes greater than $\|\theta_{\mathcal{B}d_2}^T V_{d_2}\|_1$, meaning that the same mutation ($\|V_{d_1}\|_2 = \|V_{d_2}\|_2$) may have a more significant effect on the output when it is performed on inputs of \mathcal{A} whose dimension d_1 is larger.

7.4 Exploring The Size of \mathcal{S}

Synthesizing ADIs requires preparing a sample dataset \mathcal{S} that follows the distribution of \mathcal{B} 's standard inputs. $|\mathcal{S}|$ is 20 for the above experiments, meaning that we *randomly* select 20 sample inputs from the test dataset of \mathcal{B} to form \mathcal{S} . This section explores how $|\mathcal{S}|$ influences ADI synthesis.

We launch the study using MNIST over two participants \mathcal{A} and \mathcal{B} . In particular, we randomly select ten $X_{\mathcal{A}}^*$ as the inputs of \mathcal{A} . These ten $X_{\mathcal{A}}^*$ will be classified into labels 0–9 and we confirm that they behave normally and do not dominate the joint inference. We further launch the gradient-based ADI synthesis with bounded mutation to generate an ADI from each $X_{\mathcal{A}}^*$. Model configuration and

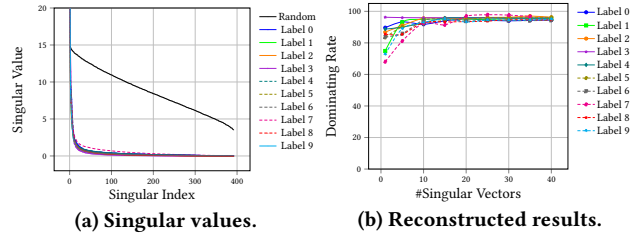


Figure 9: Singular values and reconstructed results using different numbers of singular vectors.

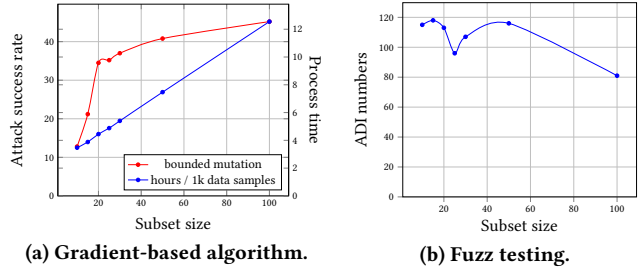


Figure 10: Performance under different subset size.

the feature partition ratio over \mathcal{A} and \mathcal{B} are aligned with evaluation in Sec. 7.1, and the dominating threshold is set as 95%.

Recall to synthesize an ADI from $X_{\mathcal{A}}^*$, we iterate each data $X_{\mathcal{B}}^i$ in \mathcal{S} and compute a perturbation vector V_i (see Alg. 1). Each V_i points toward the direction of the adversary-specified classification region $R_{i,target}$. Let h be the size of \mathcal{S} , to quantify the correlation between h perturbation vectors, we first define the matrix: $N = \begin{bmatrix} V_1 & \dots & V_h \\ \|V_1\|_2 & \dots & \|V_h\|_2 \end{bmatrix}$.

To analyze the correlation of perturbation vectors, we start by randomly selecting $h = 1000$ samples from \mathcal{B} 's dataset and use their corresponding perturbation vectors to form matrix N and report the singular values in Fig. 9a. Compared with the matrix uniformly sampled at random from the unit sphere, singular values of N decay much faster. This illustrates the existence of primary correlations and redundancies in mutations launched during ADI synthesis using different inputs of \mathcal{B} . Furthermore, this suggests that there exists a low dimensional subspace that can sufficiently capture the correlations among different inputs of \mathcal{B} .

We thus hypothesize that ADI exists because of a low-dimensional subspace that captures correlations between different classification regions. To test our hypothesis, we reconstruct the mutation using different numbers of singular vectors in decreasing order of their singular values and test the ADI dominating rates by perturbing $X_{\mathcal{A}}^*$. Fig. 9b reports the evaluation results: mutations reconstructed using only one singular vector already reach high dominating rates (over 60.0%), and ten singular vectors with the highest singular values obtain close to 95.0% dominating rates. We interpret that the results support our hypothesis. This hypothesis also explains that most perturbations are heading to a similar direction. Therefore, we do not need a large $|\mathcal{S}|$ to successfully generate ADIs.

We further evaluate how different $|\mathcal{S}|$ influences the generation of ADIs, whose results are in Fig. 10. The gradient-based ADI generation follows Sec. 7.1. Similarly, we launch a 12-hour fuzzing for different $|\mathcal{S}|$ and record the number of detected ADIs. As expected, Fig. 10a shows that larger $|\mathcal{S}|$ leads to increased success rates in

Table 7: Dominating rate of the original datasets under different numbers of participants.

#Participants	Dominating Rate	Model Accuracy
2	0.87%	97.78%
3	0.00%	95.97%
5	0.00%	97.84%

synthesizing ADIs. However, as seen in the blue line of Fig. 10a, ADI synthesis takes substantially longer time as $|\mathcal{S}|$ increases (we report the total time taken by perturbing 1,000 inputs of \mathcal{A}). Recall given a normal input of \mathcal{A} , we iterate every element in \mathcal{S} to compute the perturbation vector, which explains the linear growth of processing time in Fig. 10a. We have similar observations in Fig. 10b. Overall, while larger $|\mathcal{S}|$ may increase the likelihood of generating ADIs (as seen in Fig. 10a), it may also limit the fuzzing throughput. It is seen that the “sweet spot” is around 15–20 in Fig. 10b.

For datasets like MNIST with medium complexity (compared with relatively simple classification tasks like Credit and larger-scale tasks like NUS-WIDE), maintaining \mathcal{S} with 20 elements would well balance the cost and effectiveness. Determining the size of \mathcal{S} should take the VFL task specification, feature dimensions, and protocol complexity into account. Moreover, we emphasize that synthesizing ADIs does not require a large \mathcal{S} : as in Fig. 9a, perturbations applied toward different data samples are highly correlated.

7.5 Exploring Number of Participants

As introduced in Sec. 2, the numbers of participants in most VFL system designs are two. We now benchmark the attack effectiveness regarding different number of participants. At this step, we use the MNIST dataset and extend the SplitNN protocol for multiple participants (i.e., 3 and 5).

MNIST images are sparse: pixels close to the image corner/border are usually “dark,” conveying trivial information. To ensure that image features are partitioned evenly among participants, we divide an image into columns based on the average numbers of pixels greater than zero in each column. This way, to partition images for three participants, \mathcal{A} receives the leftmost 11 columns, participant \mathcal{B}_1 gets the middle six, while participant \mathcal{B}_2 gets the rightmost 11. For five participants, \mathcal{A} gets the leftmost eight, \mathcal{B}_{1-3} equally split the next 12 columns, and \mathcal{B}_4 gets the rightmost eight.

We take 95% as the threshold for this study. We report model accuracy and dominating rates of \mathcal{A} ’s normal inputs in Table 7. We interpret \mathcal{A} ’s normal inputs have a trivial dominating rate, which is consistent with our findings in Table 3. We further report the performance of gradient- and fuzzing-based algorithms in Table 8. Because data features are evenly partitioned among participants, the dimension of data features held by \mathcal{A} shrinks as #participants grows. Thus, the second and third columns of Table 8 show substantially lower success rates. Similarly, fuzz testing can find fewer ADIs during 12 hours. Having more participants means having fewer features allocated to each (malicious) participant. That is, the findings in Table 8 are consistent with those in Table 6 and Sec. 7.3.

8 DISCUSSION

Mitigation. Synthesizing ADIs requires to obtain a small sample dataset \mathcal{S} and to access trained VFL models on an adversarial-controlled participant. Sec. 3.2 has clarified the threat model as practical; the attack feasibility has also been demonstrated in recent

Table 8: Performance of gradient- and fuzz testing-based algorithms w.r.t. different numbers of participants.

#Participants	Gradient Random	Gradient Bounded	Fuzz Testing
2	92.9%	34.5%	113
3	56.0%	9.40%	44
5	48.0%	3.20%	9

VFL privacy inference attacks [56, 83]. The proposed attack could be mitigated by hiding the trained models, e.g., using homomorphic encryption (HE) to encrypt the trained model [32]. However, it is shown that HE is far beyond practical to secure real-world VFL protocols [94]. In addition, as stated in related work [56], hiding trained models makes model interpretation infeasible, which is undesirable in some real-world scenarios. It should also be possible to detect ADIs by training an anomaly detector to flag outlier updates from participants. In general, we anticipate to train an anomaly detector, deployed at the central server, using intermediate local model results uploaded from participants during VFL training. Then, during VFL inference, when the adversary-controlled participant uploads intermediate local model results to the central server, the deployed detector can identify outliers with high probability, especially when ADIs are synthesized using random mutation. However, as we have illustrated in Sec. 7.1 and Fig. 5, ADIs generated by bounded mutation would mostly follow the distribution of the original datasets, making them visually similar to normal inputs and hard to detect. This illustrates the stealth of our proposed attacks. Overall, we leave it as an important future direction to explore detecting ADIs with high accuracy.

Attack with Random Inputs. Careful readers may wonder whether adversarial participant \mathcal{A} can simply use random inputs to attack. Although random inputs can affect the joint inference in an undesirable manner (and presumably reduce the VFL model accuracy), we argue that random inputs are less profitable than ADIs for two reasons. First, ADIs allow to specify an adversary-targeted label l_{target} (see Sec. 4), whereas random inputs simply “muddle” the joint prediction. More importantly, random inputs can hardly nullify benign participants’ contributions, while ADIs mostly negate features contributed by benign participants, thus hogging the rewards provided to incentivize participants.

Selection of \mathcal{S} . In our evaluation, we select \mathcal{S} from the test dataset of participant \mathcal{B} randomly. According to our analysis in Sec. 4.1 and our evaluation, we don’t have strict requirements for \mathcal{S} ; randomly selecting \mathcal{S} is sufficient to synthesize ADIs. However, if \mathcal{S} is highly biased (e.g., the labels of samples in \mathcal{S} are the same), then the success rate would be lower. In practice, attackers can manually check the distribution of \mathcal{S} to avoid a highly biased situation.

Attack on Tree-based Models. This paper examines parameterized VFL systems. In tree-based VFL systems [21, 85], the structure of the malicious participant’s tree is explicitly revealed, allowing him to easily modify his inputs to reach the target node of his tree and control the output at his will. However, if some inputs never reach the malicious participant’s node, he cannot dominate the outputs of those inputs. We deem it an interesting future work to study ADIs in tree-based VFL.

9 CONCLUSION

This paper exploits VFL system using ADIs. ADIs control the joint inference and diminish benign clients’ contribution. We rigorously

prove that ADIs exist in common VFL systems. We propose gradient-based methods to synthesize ADIs in whitebox and blackbox scenarios. We also propose a greybox fuzzing testing framework for developers to perform in-house quality assurance and vulnerability assessment. We assess the impact of various settings on ADI generation. Our study exposes new VFL attack vectors, promoting early detection of unknown threats and more secure VFL systems.

REFERENCES

- [1] [n. d.]. Credit Dataset. <https://archive.ics.uci.edu/ml/datasets/default+of+credit+card+clients>.
- [2] [n. d.]. CrypTen. <https://github.com/facebookresearch/CrypTen>.
- [3] [n. d.]. PySyft. <https://github.com/OpenMined/PySyft>.
- [4] [n. d.]. TensorFlow Federated: Machine Learning on Decentralized Data. <https://www.tensorflow.org/federated>.
- [5] [n. d.]. Vehicle. [https://archive.ics.uci.edu/ml/datasets/Statlog+\(Vehicle+Silhouettes\)](https://archive.ics.uci.edu/ml/datasets/Statlog+(Vehicle+Silhouettes)).
- [6] [n. d.]. Visual Question Answering in the Medical Domain. <https://www.imageclef.org/2020/medical/vqa>.
- [7] 2020. FATE: An Industrial Grade Federated Learning Framework. www.fedai.org.
- [8] Stanislaw Antol, Aishwarya Agrawal, Jiasen Lu, Margaret Mitchell, Dhruv Batra, C. Lawrence Zitnick, and Devi Parikh. 2015. VQA: Visual Question Answering. In *International Conference on Computer Vision (ICCV)*.
- [9] Anish Athalye, Logan Engstrom, Andrew Ilyas, and Kevin Kwok. 2018. Synthesizing robust adversarial examples. In *International conference on machine learning*. PMLR, 284–293.
- [10] Eugene Bagdasaryan, Andreas Veit, Yiqing Hua, Deborah Estrin, and Vitaly Shmatikov. 2018. How to backdoor federated learning. In *International Conference on Artificial Intelligence and Statistics*. PMLR, 2938–2948.
- [11] Radu Banabic and George Candea. 2012. Fast black-box testing of system recovery code. In *Proceedings of the 7th ACM european conference on Computer Systems*. 281–294.
- [12] Mohamed Ishmael Belghazi, Aristide Baratin, Sai Rajeshwar, Sherjil Ozair, Yoshua Bengio, Aaron Courville, and Devon Hjelm. 2018. Mutual information neural estimation. In *International Conference on Machine Learning*. PMLR, 531–540.
- [13] James Henry Bell, Kallista A Bonawitz, Adrià Gascón, Tancrede Lepoint, and Mariana Raykova. 2020. Secure single-server aggregation with (poly) logarithmic overhead. In *Proceedings of the 2020 ACM SIGSAC Conference on Computer and Communications Security*. 1253–1269.
- [14] Arjun Nitin Bhagoji, Supriyo Chakraborty, Prateek Mittal, and Seraphin Calo. 2019. Analyzing federated learning through an adversarial lens. In *International Conference on Machine Learning*. PMLR, 634–643.
- [15] Keith Bonawitz, Hubert Eichner, Wolfgang Grieskamp, Dzmitry Huba, Alex Ingerman, Vladimir Ivanov, Chloe Kiddon, Jakub Konečný, Stefano Mazzocchi, H Brendan McMahan, et al. 2019. Towards federated learning at scale: System design. *arXiv preprint arXiv:1902.01046* (2019).
- [16] Keith Bonawitz, Vladimir Ivanov, Ben Kreuter, Antonio Marcedone, H Brendan McMahan, Sarvar Patel, Daniel Ramage, Aaron Segal, and Karn Seth. 2017. Practical secure aggregation for privacy-preserving machine learning. In *Proceedings of the 2017 ACM SIGSAC Conference on Computer and Communications Security*. 1175–1191.
- [17] Zhenkun Cai, Xiao Yan, Yidi Wu, Kaihao Ma, James Cheng, and Fan Yu. 2021. DGCL: An Efficient Communication Library for Distributed GNN Training. In *Proceedings of the Sixteenth European Conference on Computer Systems* (Online Event, United Kingdom) (*EuroSys '21*). Association for Computing Machinery, New York, NY, USA, 130–144. <https://doi.org/10.1145/3447786.3456233>
- [18] Zheng Chai, Hannan Fayyaz, Zeshan Fayyaz, Ali Anwar, Yi Zhou, Nathalie Baracaldo, Heiko Ludwig, and Yue Cheng. 2019. Towards taming the resource and data heterogeneity in federated learning. In *2019 {USENIX} Conference on Operational Machine Learning (OpML 19)*. 19–21.
- [19] Ashutosh Chaubey, Nikhil Agrawal, Kavya Barnwal, Keerat K Guliani, and Pramod Mehta. 2020. Universal Adversarial Perturbations: A Survey. *arXiv preprint arXiv:2005.08087* (2020).
- [20] Pin-Yu Chen, Huan Zhang, Yash Sharma, Jinfeng Yi, and Cho-Jui Hsieh. 2017. Zoo: Zeroth order optimization based black-box attacks to deep neural networks without training substitute models. In *Proceedings of the 10th ACM workshop on artificial intelligence and security*. 15–26.
- [21] Kewei Cheng, Tao Fan, Yilun Jin, Yang Liu, Tianjian Chen, Dimitrios Papadopoulos, and Qiang Yang. 2021. Secureboost: A lossless federated learning framework. *IEEE Intelligent Systems* (2021).
- [22] Tat-Seng Chua, Jinhui Tang, Richang Hong, Haojie Li, Zhiping Luo, and Yantao Zheng. 2009. NUS-WIDE: a real-world web image database from National University of Singapore. In *Proceedings of the ACM international conference on image and video retrieval*. 1–9.
- [23] Henggang Cui, Hao Zhang, Gregory R. Ganger, Phillip B. Gibbons, and Eric P. Xing. 2016. GeePS: Scalable Deep Learning on Distributed GPUs with a GPU-Specialized Parameter Server. In *Proceedings of the Eleventh European Conference on Computer Systems* (London, United Kingdom) (*EuroSys '16*). Association for Computing Machinery, New York, NY, USA, Article 4, 16 pages. <https://doi.org/10.1145/2901318.2901323>
- [24] Anirban Das and Stacy Patterson. 2021. Multi-tier federated learning for vertically partitioned data. In *ICASSP 2021-2021 IEEE International Conference on Acoustics, Speech and Signal Processing (ICASSP)*. IEEE, 3100–3104.
- [25] Arthur P Dempster, Nan M Laird, and Donald B Rubin. 1977. Maximum likelihood from incomplete data via the EM algorithm. *Journal of the Royal Statistical Society: Series B (Methodological)* 39, 1 (1977), 1–22.
- [26] Paul Adrien Maurice Dirac. 1981. *The principles of quantum mechanics*. Number 27. Oxford university press.
- [27] Minghong Fang, Xiaoyu Cao, Jinyuan Jia, and Neil Gong. 2020. Local model poisoning attacks to Byzantine-robust federated learning. In *29th {USENIX} Security Symposium ({USENIX} Security 20)*. 1605–1622.
- [28] Li Fei-Fei, Rob Fergus, and Pietro Perona. 2006. One-shot learning of object categories. *IEEE transactions on pattern analysis and machine intelligence* 28, 4 (2006), 594–611.
- [29] Ruth C Fong and Andrea Vedaldi. 2017. Interpretable explanations of black boxes by meaningful perturbation. In *Proceedings of the IEEE International Conference on Computer Vision*. 3429–3437.
- [30] Clement Fung, Chris JM Yoon, and Ivan Beschastnikh. 2018. Mitigating sybils in federated learning poisoning. *arXiv preprint arXiv:1808.04866* (2018).
- [31] Clement Fung, Chris JM Yoon, and Ivan Beschastnikh. 2020. The Limitations of Federated Learning in Sybil Settings. In *23rd International Symposium on Research in Attacks, Intrusions and Defenses ({RAID} 2020)*. 301–316.
- [32] Craig Gentry. 2009. Fully homomorphic encryption using ideal lattices. In *Proceedings of the forty-first annual ACM symposium on Theory of computing*. 169–178.
- [33] Oded Goldreich. 1998. Secure multi-party computation. *Manuscript. Preliminary version 78* (1998).
- [34] Ian Goodfellow, Yoshua Bengio, Aaron Courville, and Yoshua Bengio. 2016. *Deep learning*. Vol. 1. MIT press Cambridge.
- [35] Ian J Goodfellow, Jonathon Shlens, and Christian Szegedy. 2014. Explaining and harnessing adversarial examples. *arXiv preprint arXiv:1412.6572* (2014).
- [36] Yash Goyal, Tejas Khot, Douglas Summers-Stay, Dhruv Batra, and Devi Parikh. 2017. Making the v in VQA Matter: Elevating the Role of Image Understanding in Visual Question Answering. In *Proceedings of the IEEE Conference on Computer Vision and Pattern Recognition (CVPR)*.
- [37] Christian Grossmann, Hans-Görg Roos, and Martin Stynes. 2007. *Numerical treatment of partial differential equations*. Vol. 154. Springer.
- [38] Chuan Guo, Jacob Gardner, Yurong You, Andrew Gordon Wilson, and Kilian Weinberger. 2019. Simple black-box adversarial attacks. In *International Conference on Machine Learning*. PMLR, 2484–2493.
- [39] Otkrist Gupta and Ramesh Raskar. 2018. Distributed learning of deep neural network over multiple agents. *Journal of Network and Computer Applications* 116 (2018), 1–8.
- [40] Stephen Hardy, Wilko Henecka, Hamish Ivey-Law, Richard Nock, Giorgio Patrini, Guillaume Smith, and Brian Thorne. 2017. Private federated learning on vertically partitioned data via entity resolution and additively homomorphic encryption. *arXiv preprint arXiv:1711.10677* (2017).
- [41] Chaoyang He, Songze Li, Jinhyun So, Mi Zhang, Hongyi Wang, Xiaoyang Wang, Praneeth Vepakomma, Abhishek Singh, Hang Qiu, Li Shen, Peilin Zhao, Yan Kang, Yang Liu, Ramesh Raskar, Qiang Yang, Murali Annamaram, and Salman Avestimehr. 2020. FedML: A Research Library and Benchmark for Federated Machine Learning. *arXiv preprint arXiv:2007.13518* (2020).
- [42] Karl Moritz Hermann, Tomáš Kočíský, Edward Grefenstette, Lasse Espeholt, Will Kay, Mustafa Suleyman, and Phil Blunsom. 2015. Teaching machines to read and comprehend. *arXiv preprint arXiv:1506.03340* (2015).
- [43] R Devon Hjelm, Alex Fedorov, Samuel Lavoie-Marchildon, Karan Grewal, Phil Bachman, Adam Trischler, and Yoshua Bengio. 2018. Learning deep representations by mutual information estimation and maximization. *arXiv preprint arXiv:1808.06670* (2018).
- [44] Andrew Ilyas, Logan Engstrom, Anish Athalye, and Jessy Lin. 2018. Black-box adversarial attacks with limited queries and information. In *International Conference on Machine Learning*. PMLR, 2137–2146.
- [45] Yann LeCun, Léon Bottou, Yoshua Bengio, and Patrick Haffner. 1998. Gradient-based learning applied to document recognition. *Proc. IEEE* 86, 11 (1998), 2278–2324.
- [46] Jaehoon Lee, Yasaman Bahri, Roman Novak, Samuel S Schoenholz, Jeffrey Pennington, and Jascha Sohl-Dickstein. 2017. Deep neural networks as gaussian processes. *arXiv preprint arXiv:1711.00165* (2017).
- [47] Mu Li, David G Andersen, Alexander J Smola, and Kai Yu. 2014. Communication efficient distributed machine learning with the parameter server. *Advances in Neural Information Processing Systems 27* (2014), 19–27.
- [48] Tian Li, Maziar Sanjabi, Ahmad Beirami, and Virginia Smith. 2019. Fair resource allocation in federated learning. *arXiv preprint arXiv:1905.10497* (2019).

- [49] Xiujun Li, Xi Yin, Chunyuan Li, Pengchuan Zhang, Xiaowei Hu, Lei Zhang, Lijuan Wang, Houdong Hu, Li Dong, Furu Wei, et al. 2020. Oscar: Object-semantics aligned pre-training for vision-language tasks. In *European Conference on Computer Vision*. Springer, 121–137.
- [50] Tsung-Yi Lin, Michael Maire, Serge Belongie, James Hays, Pietro Perona, Deva Ramanan, Piotr Dollár, and C Lawrence Zitnick. 2014. Microsoft COCO: Common objects in context. In *European conference on computer vision*. Springer, 740–755.
- [51] Fenglin Liu, Xian Wu, Shen Ge, Wei Fan, and Yuexian Zou. 2020. Federated Learning for Vision-and-Language Grounding Problems.. In *AAAI*. 11572–11579.
- [52] Yang Liu, Zhihao Yi, and Tianjian Chen. 2020. Backdoor attacks and defenses in feature-partitioned collaborative learning. *arXiv preprint arXiv:2007.03608* (2020).
- [53] Jiaseen Lu, Jianwei Yang, Dhruv Batra, and Devi Parikh. 2016. Hierarchical question-image co-attention for visual question answering. *arXiv preprint arXiv:1606.00061* (2016).
- [54] A Lubna, Saidalavi Kalady, and A Lijiya. 2019. MoBVQA: A Modality based Medical Image Visual Question Answering System. In *TENCON 2019-2019 IEEE Region 10 Conference (TENCON)*. IEEE, 727–732.
- [55] Jeffrey F Lukman, Huan Ke, Cesar A Stuardo, Riza O Suminto, Danian H Kurniawan, Dikaimin Simon, Satria Priambada, Chen Tian, Feng Ye, Tanakorn Leesatapornwongsa, et al. 2019. Flymc: Highly scalable testing of complex interleavings in distributed systems. In *Proceedings of the Fourteenth EuroSys Conference 2019*. 1–16.
- [56] Xinjian Luo, Yuncheng Wu, Xiaokui Xiao, and Beng Chin Ooi. 2020. Feature Inference Attack on Model Predictions in Vertical Federated Learning. *arXiv preprint arXiv:2010.10152* (2020).
- [57] Xinjian Luo, Yuncheng Wu, Xiaokui Xiao, and Beng Chin Ooi. 2021. Feature inference attack on model predictions in vertical federated learning. In *2021 IEEE 37th International Conference on Data Engineering (ICDE)*. IEEE, 181–192.
- [58] Alireza Makhzani, Jonathon Shlens, Navdeep Jaitly, Ian Goodfellow, and Brendan Frey. 2015. Adversarial autoencoders. *arXiv preprint arXiv:1511.05644* (2015).
- [59] Ismael Martinez, Sreya Francis, and Abdelhakim Senhaji Hafid. 2019. Record and reward federated learning contributions with blockchain. In *2019 International Conference on Cyber-Enabled Distributed Computing and Knowledge Discovery (CyberC)*. IEEE, 50–57.
- [60] Geoffrey J McLachlan and Kaye E Basford. 1988. *Mixture models: Inference and applications to clustering*. Vol. 38. M. Dekker New York.
- [61] Brendan McMahan, Eider Moore, Daniel Ramage, Seth Hampson, and Blaise Aguerre y Arcas. 2017. Communication-efficient learning of deep networks from decentralized data. In *Artificial Intelligence and Statistics*. PMLR, 1273–1282.
- [62] Seyed-Mohsen Moosavi-Dezfooli, Alhussein Fawzi, Omar Fawzi, and Pascal Frossard. 2017. Universal adversarial perturbations. In *Proceedings of the IEEE conference on computer vision and pattern recognition*. 1765–1773.
- [63] Nina Narodytska and Shiva Prasad Kasiviswanathan. 2016. Simple black-box adversarial perturbations for deep networks. *arXiv preprint arXiv:1612.06299* (2016).
- [64] Milad Nasr, Reza Shokri, and Amir Houmansadr. 2019. Comprehensive privacy analysis of deep learning: Passive and active white-box inference attacks against centralized and federated learning. In *2019 IEEE symposium on security and privacy (SP)*. IEEE, 739–753.
- [65] Richard Nock, Stephen Hardy, Wilko Henecka, Hamish Ivey-Law, Giorgio Patrini, Guillaume Smith, and Brian Thorne. 2018. Entity resolution and federated learning get a federated resolution. *arXiv preprint arXiv:1803.04035* (2018).
- [66] Kexin Pei, Yinzhi Cao, Junfeng Yang, and Suman Jana. 2017. DeepXplore: Automated Whitebox Testing of Deep Learning Systems. In *Proceedings of the 26th Symposium on Operating Systems Principles (Shanghai, China) (SOSP '17)*. Association for Computing Machinery, New York, NY, USA, 1–18. <https://doi.org/10.1145/3132747.3132785>
- [67] Yanghua Peng, Yixin Bao, Yangrui Chen, Chuan Wu, and Chuanxiong Guo. 2018. Optimus: An Efficient Dynamic Resource Scheduler for Deep Learning Clusters. In *Proceedings of the Thirteenth EuroSys Conference (Porto, Portugal) (EuroSys '18)*. Association for Computing Machinery, New York, NY, USA, Article 3, 14 pages. <https://doi.org/10.1145/3190508.3190517>
- [68] Krishna Pillutla, Sham M Kakade, and Zaid Harchaoui. 2019. Robust aggregation for federated learning. *arXiv preprint arXiv:1912.13445* (2019).
- [69] Foster J Provost and Daniel N Hennessy. 1996. Scaling up: Distributed machine learning with cooperation. In *AAAI/IAAI, Vol. 1*. Citeseer, 74–79.
- [70] Shaoqing Ren, Kaiming He, Ross Girshick, and Jian Sun. 2016. Faster R-CNN: Towards real-time object detection with region proposal networks. *IEEE transactions on pattern analysis and machine intelligence* 39, 6 (2016), 1137–1149.
- [71] Monica Scannapieco, Ilya Figotin, Elisa Bertino, and Ahmed K Elmagarmid. 2007. Privacy preserving schema and data matching. In *Proceedings of the 2007 ACM SIGMOD international conference on Management of data*. 653–664.
- [72] Avanti Shrikumar, Peyton Greenside, and Anshul Kundaje. 2017. Learning important features through propagating activation differences. In *International Conference on Machine Learning*. PMLR, 3145–3153.
- [73] Rachael Hwee Ling Sim, Yehong Zhang, Mun Choon Chan, and Bryan Kian Hsiang Low. 2020. Collaborative machine learning with incentive-aware model rewards. In *International Conference on Machine Learning (ICML)*. PMLR, 8927–8936.
- [74] Tianshu Song, Yongxin Tong, and Shuyue Wei. 2019. Profit allocation for federated learning. In *2019 IEEE International Conference on Big Data (Big Data)*. IEEE, 2577–2586.
- [75] Ziteng Sun, Peter Kairouz, Ananda Theertha Suresh, and H Brendan McMahan. 2019. Can you really backdoor federated learning? *arXiv preprint arXiv:1911.07963* (2019).
- [76] Fnu Suya, Jianfeng Chi, David Evans, and Yuan Tian. 2020. Hybrid Batch Attacks: Finding Black-box Adversarial Examples with Limited Queries. In *29th USENIX Security Symposium (USENIX Security 20)*. USENIX Association, 1327–1344. <https://www.usenix.org/conference/usenixsecurity20/presentation/suya>
- [77] Vale Tolpegin, Stacey Truex, Mehmet Emre Gursoy, and Ling Liu. 2020. Data poisoning attacks against federated learning systems. In *European Symposium on Research in Computer Security*. Springer, 480–501.
- [78] Kentaro Toyoda and Allan N Zhang. 2019. Mechanism design for an incentive-aware blockchain-enabled federated learning platform. In *2019 IEEE International Conference on Big Data (Big Data)*. IEEE, 395–403.
- [79] Florian Tramèr, Alexey Kurakin, Nicolas Papernot, Ian Goodfellow, Dan Boneh, and Patrick McDaniel. 2017. Ensemble adversarial training: Attacks and defenses. *arXiv preprint arXiv:1705.07204* (2017).
- [80] Hongyi Wang, Kartik Sreenivasan, Shashank Rajput, Harit Vishwakarma, Saurabh Agarwal, Jy-yong Sohn, Kangwook Lee, and Dimitris Papailiopoulos. 2020. Attack of the tails: Yes, you really can backdoor federated learning. *Advances in Neural Information Processing Systems* 33 (2020).
- [81] Lei Wang, Qiang Yin, Chao Tian, Jianbang Yang, Rong Chen, Wenyuan Yu, Zihang Yao, and Jingren Zhou. 2021. FlexGraph: A Flexible and Efficient Distributed Framework for GNN Training. In *Proceedings of the Sixteenth European Conference on Computer Systems (Online Event, United Kingdom) (EuroSys '21)*. Association for Computing Machinery, New York, NY, USA, 67–82. <https://doi.org/10.1145/3447786.3456229>
- [82] Zhibo Wang, Mengkai Song, Zhifei Zhang, Yang Song, Qian Wang, and Hairong Qi. 2019. Beyond inferring class representatives: User-level privacy leakage from federated learning. In *IEEE INFOCOM 2019-IEEE Conference on Computer Communications*. IEEE, 2512–2520.
- [83] Haiqin Weng, Juntao Zhang, Feng Xue, Tao Wei, Shouling Ji, and Zhiyuan Zong. 2020. Privacy Leakage of Real-World Vertical Federated Learning. *arXiv preprint arXiv:2011.09290* (2020).
- [84] David J Wu, Joe Zimmerman, Jérémy Planul, and John C Mitchell. 2016. Privacy-preserving shortest path computation (NDSS).
- [85] Yuncheng Wu, Shaofeng Cai, Xiaokui Xiao, Gang Chen, and Beng Chin Ooi. 2020. Privacy preserving vertical federated learning for tree-based models. *arXiv preprint arXiv:2008.06170* (2020).
- [86] Wensheng Xia, Ying Li, Lan Zhang, Zhonghai Wu, and Xiaoyong Yuan. 2021. A Vertical Federated Learning Framework for Horizontally Partitioned Labels. *arXiv preprint arXiv:2106.10056* (2021).
- [87] Chulin Xie, Keli Huang, Pin-Yu Chen, and Bo Li. 2019. DBA: Distributed Backdoor Attacks against Federated Learning. In *International Conference on Learning Representations*.
- [88] Xiaofei Xie, Lei Ma, Felix Juefei-Xu, Minhui Xue, Hongxu Chen, Yang Liu, Jianjun Zhao, Bo Li, Jianxiong Yin, and Simon See. 2019. DeepHunter: A Coverage-Guided Fuzz Testing Framework for Deep Neural Networks. In *Proceedings of the 28th ACM SIGSOFT International Symposium on Software Testing and Analysis (Beijing, China) (ISSTA 2019)*. Association for Computing Machinery, New York, NY, USA, 146–157. <https://doi.org/10.1145/3293882.3330579>
- [89] Qiang Yang, Yang Liu, Tianjian Chen, and Yongxin Tong. 2019. Federated machine learning: Concept and applications. *ACM Transactions on Intelligent Systems and Technology (TIST)* 10, 2 (2019), 1–19.
- [90] Shuo Yang, Fan Wu, Shaojie Tang, Xiaofeng Gao, Bo Yang, and Guihai Chen. 2017. On designing data quality-aware truth estimation and surplus sharing method for mobile crowdsensing. *IEEE Journal on Selected Areas in Communications* 35, 4 (2017), 832–847.
- [91] Han Yu, Zelei Liu, Yang Liu, Tianjian Chen, Mingshu Cong, Xi Weng, Dusit Niyato, and Qiang Yang. 2020. A fairness-aware incentive scheme for federated learning. In *Proceedings of the AAAI/ACM Conference on AI, Ethics, and Society*. 393–399.
- [92] Xinhao Yuan and Junfeng Yang. 2020. Effective Concurrency Testing for Distributed Systems. In *Proceedings of the Twenty-Fifth International Conference on Architectural Support for Programming Languages and Operating Systems (Lausanne, Switzerland) (ASPLOS '20)*. Association for Computing Machinery, New York, NY, USA, 1141–1156. <https://doi.org/10.1145/3373376.3378484>
- [93] Michał Zalewski. 2021. American Fuzzy Lop. <https://lcamtuf.coredump.cx/afl/>.
- [94] Chengliang Zhang, Suyi Li, Junzhe Xia, Wei Wang, Feng Yan, and Yang Liu. 2020. Batchcrypt: Efficient homomorphic encryption for cross-silo federated learning. In *2020 {USENIX} Annual Technical Conference ({USENIX}) {ATC} 20*. 493–506.

[95] Song Chun Zhu and Alan Yuille. 1996. Region competition: Unifying snakes, region growing, and Bayes/MDL for multiband image segmentation. *IEEE transactions on pattern analysis and machine intelligence* 18, 9 (1996), 884–900.

APPENDIX

A TRAINING AND IMPLEMENTATION DETAILS OF LEARNING PROTOCOLS

HeteroLR. Given n training samples X_i whose label is $y_i \in \{0, 1\}$ and coefficient vector θ , logistic regression can be described in a basic form as follows:

$$\mathbb{P}(y_i = 1|X_i, \theta) = h_\theta(X_i) = \frac{1}{1 + e^{-\theta^T X_i}} \quad (3)$$

In typical VFL settings, X_i is partitioned as $[X_A^i || X_B^i]$, while θ is partitioned as $[\theta_A || \theta_B]$. Therefore, HeteroLR in VFL can be formulated as follows:

$$\begin{aligned} \mathbb{P}(y_i = 1|X_A^i, X_B^i, \theta_A, \theta_B) &= h_{\theta_A, \theta_B}(X_A^i, X_B^i) \\ &= \frac{1}{1 + e^{-\theta_A^T X_A^i - \theta_B^T X_B^i}} \end{aligned} \quad (4)$$

whose training objective is to minimize the loss function:

$$\begin{aligned} \mathbb{L}_\theta &= -\frac{1}{n} \sum_{i=1}^n y_i \log(h_{\theta_A, \theta_B}(X_A^i, X_B^i)) \\ &\quad + (1 - y_i) \log(1 - h_{\theta_A, \theta_B}(X_A^i, X_B^i)) \end{aligned} \quad (5)$$

We have introduced the general procedure of HeteroLR in Sec. 2. At the training stage, when computing gradients, Taylor approximation and homomorphic encryption scheme can be utilized to make training more efficient. To make a joint inference for user ID i , \mathcal{C} collects local prediction results $\theta_A^T X_A^i$ and $\theta_B^T X_B^i$. It then computes and sends the probability $\frac{1}{1 + e^{-\theta_A^T X_A^i - \theta_B^T X_B^i}}$ back to \mathcal{A} and \mathcal{B} . Note that all the intermediate data is encrypted.

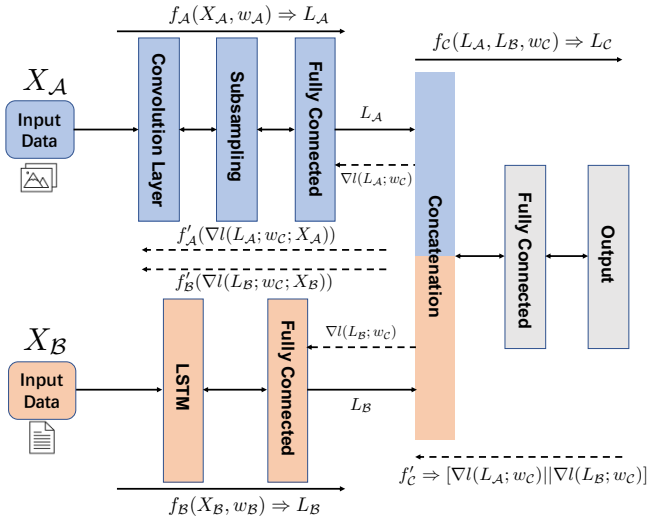


Figure 11: Architecture of SplitNN.

SplitNN. Fig. 11 depicts the architecture of heterogeneous neural network (also known as a special case of SplitNN). SplitNN

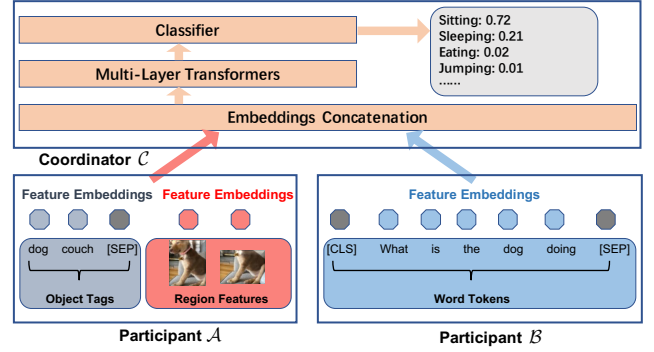


Figure 12: Architecture of VFVQA.

facilitates multiple participants holding data with different feature spaces to train a distributed model without sharing raw data. In the forward propagation phase, \mathcal{A} and \mathcal{B} compute the outputs of their local models (w_A and w_B) and forward them to the coordinator \mathcal{C} :

$$\begin{aligned} L_A &= f_A(X_A, w_A) \\ L_B &= f_B(X_B, w_B) \end{aligned} \quad (6)$$

The forwarded local outputs, L_A and L_B , will be concatenated on the coordinator side and fed to the coordinator model (w_C) for a joint inference whose result is L_C .

$$L_C = f_C([L_A || L_B], w_C) \quad (7)$$

In the backward propagation phase, the coordinator \mathcal{C} computes the gradients $f'_C(L_C)$, performs gradient descent on its model, and obtains the gradients of local outputs submitted by the participants as follows:

$$[\nabla l(L_A; w_C) || \nabla l(L_B; w_C)] = f'_C(L_C) \quad (8)$$

Back to the participant side, once receiving the gradients, the participants further compute the local gradients $f'_A(\nabla l(L_A; w_C; X_A))$ and $f'_B(\nabla l(L_B; w_C; X_B))$ and then update local models. f represents the neural network and f' represents its derivative. In the forward and backward propagations, no raw data is directly sent to the coordinator or exchanged among participants, and all intermediate data is encrypted. Furthermore, by extending the SplitNN protocol, we can construct more complex models like CNN and LSTM following the VFL paradigm.

VFVQA. Visual Question Answering [8], a popular multimodal learning task, answers open-ended natural-language questions about images. VQA models develop a joint understanding of questions and images and have been employed in privacy-sensitive scenarios like medical image diagnosis [6, 54]. VFL provides a practical and effective solution to facilitate privacy-preserving VQA [51]. In our evaluation, we modify the state-of-the-art VQA model Oscar [49] and construct VFVQA as illustrated in Fig. 12.

As introduced in Sec. 2, VFVQA concretizes and extends the SplitNN protocol, which involves considerable engineering efforts to link with several modern computer vision and natural language processing models. \mathcal{A} holds the image data and their associated object tags. It computes the feature representation of data using FasterRCNN [70] and BERT [49], where X_{A_1} and X_{A_2} represent the image data and the corresponding tags, respectively. \mathcal{B} holds the

textual data (i.e., “questions” in VQA) and computes the embedding results of each question using BERT. In particular, \mathcal{A} holds the image data and their associated object tags. It uses FasterRCNN [70] and BERT [49] to process $X_{\mathcal{A}_1}$ and $X_{\mathcal{A}_2}$, corresponding to images and tags. \mathcal{B} process the textual data (i.e., “questions” in VQA tasks) using BERT:

$$\begin{aligned} L_{\mathcal{A}} &= [\text{FasterRCNN}(X_{\mathcal{A}_1}, w_{\mathcal{A}_1}) \parallel \text{BERT}(X_{\mathcal{A}_2}, w_{\mathcal{A}_2})] \\ L_{\mathcal{B}} &= \text{BERT}(X_{\mathcal{B}}, w_{\mathcal{B}}) \end{aligned} \quad (9)$$

As specified by the SplitNN protocol, local results on each participant are sent to the coordinator \mathcal{C} . Then, \mathcal{C} predicts the answer, another natural language sentence, to the raised question on \mathcal{B} based on the image feature shared by \mathcal{A} using multi-layer transformers:

$$L_{\mathcal{C}} = \text{Transformer}([L_{\mathcal{A}} \parallel L_{\mathcal{B}}], w_{\mathcal{C}}) \quad (10)$$

The backward propagation phase is performed consistently with SplitNN. And all intermediate data in the above phases are encrypted.

B PIPELINE OF BLACKBOX ADI SYNTHESIS

In this section, we present an end-to-end illustration of ADI synthesis in the blackbox setting. We consider the VFL example given in Sec. 1, where a FinTech and a bank jointly predict a user’s credit score. Before launching the attack and synthesizing ADIs, we assume that a VFL system has been well trained, where \mathcal{A} takes training data from the FinTech and \mathcal{B} takes the training data from the bank.

Fig. 13a depicts the procedure of collecting \mathcal{S} , whose high-level procedure has been mentioned in Sec. 3.2. In particular, the malicious participant \mathcal{A} conspires with a small group of users: these users behave normally, but are willing to share their records in the bank with \mathcal{A} (①). These users behave *normally* and register their information in the bank. Their provided bank records will form our target sample dataset \mathcal{S} (②). Then, as discussed in Sec. 4.2, these users further compute another collection of bank records $X_{\mathcal{B}}^{i,k}$, by adding permutation δ_k to each bank record $X_{\mathcal{B}}^i \in \mathcal{S}$. These $X_{\mathcal{B}}^{i,k}$ form another sample dataset \mathcal{S}^* (③). Given that users are conspiring with \mathcal{A} , both \mathcal{S} and \mathcal{S}^* are shared with \mathcal{A} (④). Similarly, \mathcal{S}^* will need to be provided to the bank, and therefore, both \mathcal{S} and \mathcal{S}^* are accessible to \mathcal{B} (⑤, ⑥).

With two tiny datasets, \mathcal{S} and \mathcal{S}^* , become accessible to both \mathcal{A} and \mathcal{B} , \mathcal{A} can start to synthesize ADIs via estimated gradients (see Sec. 4.2). Fig. 13b shows the pipeline of our blackbox ADI synthesis.

Typically, before launching a joint inference, \mathcal{C} will coordinate and inform \mathcal{A} and \mathcal{B} about the user ID. Thus, \mathcal{A} can easily decide whether the current input of \mathcal{B} is from the sample set \mathcal{S} or \mathcal{S}^* according to the current user ID. If so, \mathcal{A} can start to update its ADI input $X_{\mathcal{A}}^*$. To do so, \mathcal{A} feeds ADI $X_{\mathcal{A}}^*$ to local model $M_{\mathcal{A}}$ and \mathcal{B} feeds $X_{\mathcal{B}}^i \in \mathcal{S}$ or $X_{\mathcal{B}}^{i,k} \in \mathcal{S}^*$ to local model $M_{\mathcal{B}}$ and get the corresponding outputs (①). Then, \mathcal{A} and \mathcal{B} submit their local outputs to \mathcal{C} and receive the joint inference output of the VFL model from \mathcal{C} (② and ③). Then, as we discuss in Sec. 4.2, \mathcal{A} can compute the gradients of $X_{\mathcal{B}}^i \in \mathcal{S}$ by FDM (④). Finally, \mathcal{A} updates ADI $X_{\mathcal{A}}^*$ by Alg. 1 without accessing the local model of \mathcal{B} (⑤).

C PROOF OF COROLLARY 1

Corollary 1 (Variance of HeteroLR). With fixed input $X_{\mathcal{A}}^*$ and varying input $X_{\mathcal{B}}$ following any distribution whose density function is $p(X_{\mathcal{B}})$, the output variance of HeteroLR is:

$$\begin{aligned} \mathbb{V}_{X_{\mathcal{B}} \in D_{\mathcal{B}}}(f(X_{\mathcal{A}}^*, X_{\mathcal{B}})) &= \sum_{k=1}^{\mathcal{K}} \pi_k \Phi\left(\frac{\mu'_k}{\sqrt{\sigma_1^2 + \sigma_k'^2}}\right) \left(1 - \sum_{k=1}^{\mathcal{K}} \pi_k \Phi\left(\frac{\mu'_k}{\sqrt{\sigma_1^2 + \sigma_k'^2}}\right)\right) \\ &+ \sum_{k=1}^{\mathcal{K}} \frac{\pi_k}{\sqrt{2\pi}} \frac{1}{\sqrt{\sigma_k'^2 + \sigma_2^2}} \exp\left\{-\frac{1}{2} \frac{\mu_k'^2}{\sigma_k'^2 + \sigma_2^2}\right\} \end{aligned}$$

, where the density function $p(X_{\mathcal{B}})$ is approximated by Gaussian Mixture Model: $p(X_{\mathcal{B}}) \approx \sum_{k=1}^{\mathcal{K}} \pi_k \mathcal{N}(X_{\mathcal{B}} | \mu_{\mathbf{k}}, \Sigma_{\mathbf{k}})$, $\sum_{k=1}^{\mathcal{K}} \pi_k = 1$, $\pi_k > 0$, \mathcal{K} is a finite number, $\mu_{\mathbf{k}} \in \mathbb{R}^{d_2}$, $\Sigma_{\mathbf{k}} \in \mathbb{R}^{d_2 \times d_2}$, $\mu'_k = \theta_{\mathcal{A}}^T X_{\mathcal{A}}^* + \theta_{\mathcal{B}}^T \mu_{\mathbf{k}}$, $\sigma_k'^2 = \theta_{\mathcal{B}}^T \Sigma_{\mathbf{k}} \theta_{\mathcal{B}}$, $\sigma_1 = 1.699$, and $\sigma_2 = 1.630$.

PROOF. Considering the fixed input $X_{\mathcal{A}}^*$ and varying input $X_{\mathcal{B}}$, and let $S = \theta_{\mathcal{A}}^T X_{\mathcal{A}}^* + \theta_{\mathcal{B}}^T X_{\mathcal{B}}$. Thus, $f(X_{\mathcal{A}}^*, X_{\mathcal{B}}) = g(S)$. Aligned with the conventions [12, 28, 34, 43, 46, 58, 95] in machine learning, we use Gaussian mixture model [60] and Expectation Maximization [25] to approximate the density function $p(X_{\mathcal{B}})$ as:

$$p(X_{\mathcal{B}}) \approx \sum_{k=1}^{\mathcal{K}} \pi_k \mathcal{N}(X_{\mathcal{B}} | \mu_{\mathbf{k}}, \Sigma_{\mathbf{k}}) \quad (11)$$

, where $\sum_{k=1}^{\mathcal{K}} \pi_k = 1$, $\pi_k > 0$, \mathcal{K} is a finite number, $\mu_{\mathbf{k}} \in \mathbb{R}^{d_2}$ and $\Sigma_{\mathbf{k}} \in \mathbb{R}^{d_2 \times d_2}$. Note that if $p(X_{\mathcal{B}})$ is discrete and not smooth (e.g. $X_{\mathcal{B}}$ is categorical data), we can approximate it by taking $\Sigma_{\mathbf{k}} \rightarrow 0$ and \mathcal{K} becomes the total number of distinct data in $X_{\mathcal{B}}$, the Gaussian distribution density would become a Dirac delta function [26] and the following calculations will still hold.

Further, we can obtain the density function of S as: $p(S) = \sum_{k=1}^{\mathcal{K}} \pi_k \mathcal{N}(S | \theta_{\mathcal{A}}^T X_{\mathcal{A}}^* + \theta_{\mathcal{B}}^T \mu_{\mathbf{k}}, \theta_{\mathcal{B}}^T \Sigma_{\mathbf{k}} \theta_{\mathcal{B}})$. Taking $\mu'_k = \theta_{\mathcal{A}}^T X_{\mathcal{A}}^* + \theta_{\mathcal{B}}^T \mu_{\mathbf{k}}$ and $\sigma_k'^2 = \theta_{\mathcal{B}}^T \Sigma_{\mathbf{k}} \theta_{\mathcal{B}}$, we thus calculate the expected value of the output:

$$\begin{aligned} \mathbb{E}_{X_{\mathcal{B}} \in D_{\mathcal{B}}}(g(S)) &= \int g(t) \sum_{k=1}^{\mathcal{K}} \pi_k \mathcal{N}(t | \mu'_k, \sigma_k'^2) dt \\ &\approx \int \sum_{k=1}^{\mathcal{K}} \pi_k \Phi\left(\frac{t}{\sigma_1}\right) \mathcal{N}(t | \mu'_k, \sigma_k'^2) dt \quad (12) \\ &= \sum_{k=1}^{\mathcal{K}} \pi_k \Phi\left(\frac{\mu'_k}{\sqrt{\sigma_1^2 + \sigma_k'^2}}\right) \end{aligned}$$

Here, the $g(t)$ is approximated by the cumulative distribution function of standard Gaussian distribution and parameter σ_1 as $\Phi(\frac{t}{\sigma_1})$, where $\sigma_1 = 1.699$ to minimize the L^2 error. The variance of the output is calculated as follows:

$$\begin{aligned} \mathbb{V}_{X_{\mathcal{B}} \in D_{\mathcal{B}}}(g(S)) &= \langle g(S)^2 \rangle - \langle g(S) \rangle^2 \\ &= \langle g(S) - g(S)(1 - g(S)) \rangle - \langle g(S) \rangle^2 \quad (13) \\ &= \langle g(S) \rangle (1 - \langle g(S) \rangle) - \langle g'(S) \rangle \end{aligned}$$

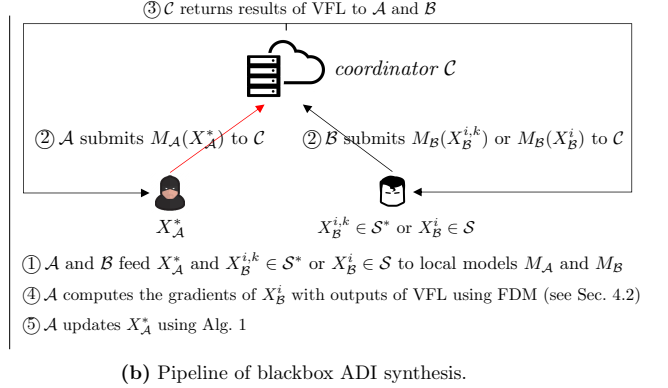
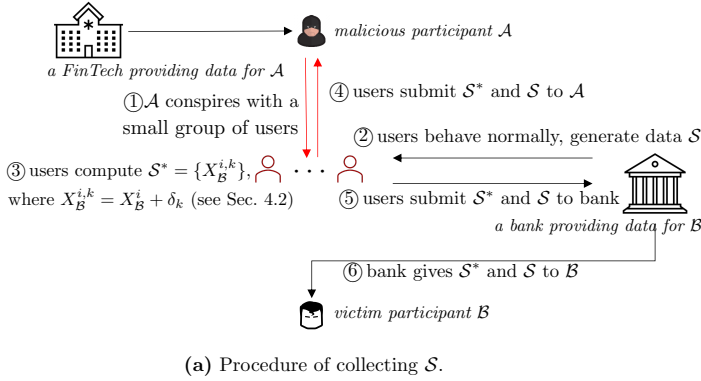


Figure 13: Pipeline of Blackbox ADI Synthesis.

, where $\langle \cdot \rangle$ donates $\mathbb{E}_{X_B \in D_B}(\cdot)$. Further, we approximate the derivation of Sigmoid function $g'(S)$ using the pdf of Gaussian distribution. When the L^2 error is minimized, we get the approximated function of $g'(S)$ with $\sigma_2 = 1.630$:

$$g'(S) \approx \frac{1}{\sqrt{2\pi}\sigma_2} \exp\left\{-\frac{S^2}{2\sigma_2^2}\right\} \quad (14)$$

Further, we can calculate the expected value of the derivation of Sigmoid function:

$$\begin{aligned} \mathbb{E}_{X_B \in D_B}(g'(S)) &= \int \sum_{k=1}^{\mathcal{K}} \frac{\pi_k}{2\pi\sigma_k'\sigma_2} \exp\left\{-\frac{t^2}{2\sigma_2^2} - \frac{(t-\mu_k')^2}{2\sigma_k'^2}\right\} dt \\ &= \sum_{k=1}^{\mathcal{K}} \frac{\pi_k}{\sqrt{2\pi}} \frac{1}{\sqrt{\sigma_k'^2 + \sigma_2^2}} \exp\left\{-\frac{1}{2} \frac{\mu_k'^2}{\sigma_k'^2 + \sigma_2^2}\right\} \end{aligned} \quad (15)$$

According to Eq. 12, Eq. 13 and Eq. 15, we can calculate the variance of logistic regression result as follows:

$$\begin{aligned} \mathbb{V}_{X_B \in D_B}(g(S)) &= \sum_{k=1}^{\mathcal{K}} -\frac{\pi_k}{\sqrt{2\pi}} \frac{1}{\sqrt{\sigma_k'^2 + \sigma_2^2}} \exp\left\{-\frac{1}{2} \frac{\mu_k'^2}{\sigma_k'^2 + \sigma_2^2}\right\} \\ &\quad + \sum_{k=1}^{\mathcal{K}} \pi_k \Phi\left(\frac{\mu_k'}{\sqrt{\sigma_1^2 + \sigma_k'^2}}\right) \left(1 - \sum_{k=1}^{\mathcal{K}} \pi_k \Phi\left(\frac{\mu_k'}{\sqrt{\sigma_1^2 + \sigma_k'^2}}\right)\right) \end{aligned} \quad (16)$$

□

D PROOF OF COROLLARY 2

Corollary 2 (Variance of SplitNN). With fixed input X_A^* and varying input X_B following any distribution whose density function is $p(X_B)$, the output variance of SplitNN is:

$$\begin{aligned} \mathbb{V}_{X_B \in D_B}(f(X_A^*, X_B)) &= \left(\sum_{k=1}^{\mathcal{K}} \pi_k \Phi\left(\frac{\mu_k'}{\sigma_k'}\right)\right) \left(\sum_{k=1}^{\mathcal{K}} \pi_k^2 \sigma_k'^2 \left(1 - \frac{\mu_k'}{\sigma_k'} \frac{\phi\left(\frac{\mu_k'}{\sigma_k'}\right)}{\Phi\left(\frac{\mu_k'}{\sigma_k'}\right)} - \left(\frac{\phi\left(\frac{\mu_k'}{\sigma_k'}\right)}{\Phi\left(\frac{\mu_k'}{\sigma_k'}\right)}\right)^2\right)\right) \\ &\quad + \left(\sum_{k=1}^{\mathcal{K}} \pi_k \left(\mu_k' + \sigma_k' \frac{\phi\left(\frac{\mu_k'}{\sigma_k'}\right)}{\Phi\left(\frac{\mu_k'}{\sigma_k'}\right)}\right)\right)^2 \left(1 - \sum_{k=1}^{\mathcal{K}} \pi_k \Phi\left(\frac{\mu_k'}{\sigma_k'}\right)\right) \end{aligned}$$

, where the density function $p(X_B)$ is approximated by Gaussian Mixture Model: $p(X_B) \approx \sum_{k=1}^{\mathcal{K}} \pi_k \mathcal{N}(X_B | \mu_k, \Sigma_k)$, $\sum_{k=1}^{\mathcal{K}} \pi_k = 1$, $\pi_k > 0$, \mathcal{K} is a finite number, $\mu_k' = w_A^T X_A^* + w_B^T \mu_k$, and $\sigma_k'^2 = w_B^T \Sigma_k w_B$.

PROOF. Similar to the proof of Corollary 1, for any distribution of X_B , we use Gaussian mixture model and Expectation Maximization to approximate its density function $p(X_B)$ as:

$$p(X_B) \approx \sum_{k=1}^{\mathcal{K}} \pi_k \mathcal{N}(X_B | \mu_k, \Sigma_k) \quad (17)$$

, where $\sum_{k=1}^{\mathcal{K}} \pi_k = 1$, $\pi_k > 0$, \mathcal{K} is a finite number, $\mu_k \in \mathbb{R}^{d_2}$ and $\Sigma_k \in \mathbb{R}^{d_2 \times d_2}$. Similarly, if $p(X_B)$ is highly discrete, we can approximate it by taking $\Sigma_k \rightarrow 0$.

For fixed X_A^* , let $Y = w_A^T X_A^* + w_B^T X_B$. Thus, $p(Y) = \sum_{k=1}^{\mathcal{K}} \pi_k \mathcal{N}(Y | \mu_k', \sigma_k'^2)$. Taking $\mu_k' = w_A^T X_A^* + w_B^T \mu_k$ and $\sigma_k'^2 = w_B^T \Sigma_k w_B$, we have:

$$\mathbb{E}_{X_B \in D_B}(Y | Y > 0) = \sum_{k=1}^{\mathcal{K}} \pi_k \left(\mu_k' + \sigma_k' \frac{\phi\left(\frac{\mu_k'}{\sigma_k'}\right)}{\Phi\left(\frac{\mu_k'}{\sigma_k'}\right)}\right) \quad (18)$$

$$\mathcal{P}(Y > 0) = \sum_{k=1}^{\mathcal{K}} \pi_k \Phi\left(\frac{\mu_k'}{\sigma_k'}\right) \quad (19)$$

And we can get the expected value of the central coordinator output:

$$\begin{aligned} \mathbb{E}_{X_B \in D_B}(f(X_A^*, X_B)) &= \mathbb{E}_{X_B \in D_B}(Y | Y > 0) \times \mathcal{P}(Y > 0) \\ &= \left(\sum_{k=1}^{\mathcal{K}} \pi_k \left(\mu_k' + \sigma_k' \frac{\phi\left(\frac{\mu_k'}{\sigma_k'}\right)}{\Phi\left(\frac{\mu_k'}{\sigma_k'}\right)}\right)\right) \left(\sum_{k=1}^{\mathcal{K}} \pi_k \Phi\left(\frac{\mu_k'}{\sigma_k'}\right)\right) \end{aligned} \quad (20)$$

The variance of the truncated mixture Gaussian distribution is:

$$\mathbb{V}_{X_B \in D_B}(Y | Y > 0) = \sum_{k=1}^{\mathcal{K}} \pi_k^2 \sigma_k'^2 \left(1 - \frac{\mu_k'}{\sigma_k'} \frac{\phi\left(\frac{\mu_k'}{\sigma_k'}\right)}{\Phi\left(\frac{\mu_k'}{\sigma_k'}\right)} - \left(\frac{\phi\left(\frac{\mu_k'}{\sigma_k'}\right)}{\Phi\left(\frac{\mu_k'}{\sigma_k'}\right)}\right)^2\right) \quad (21)$$

According to Eq. 18, 19, 20 and 21, we have:

$$\begin{aligned}
\mathbb{E}_{X_{\mathcal{B}} \in D_{\mathcal{B}}}(Y^2|Y > 0) &= \mathbb{V}_{X_{\mathcal{B}} \in D_{\mathcal{B}}}(Y|Y > 0) + (\mathbb{E}_{X_{\mathcal{B}} \in D_{\mathcal{B}}}(Y|Y > 0))^2 \\
&= \sum_{k=1}^{\mathcal{K}} \pi_k^2 \sigma_k'^2 \left(1 - \frac{\mu'_k}{\sigma'_k} \frac{\phi(\frac{\mu'_k}{\sigma'_k})}{\Phi(\frac{\mu'_k}{\sigma'_k})} - \left(\frac{\phi(\frac{\mu'_k}{\sigma'_k})}{\Phi(\frac{\mu'_k}{\sigma'_k})}\right)^2\right) \\
&\quad + \left(\sum_{k=1}^{\mathcal{K}} \pi_k \left(\mu'_k + \sigma'_k \frac{\phi(\frac{\mu'_k}{\sigma'_k})}{\Phi(\frac{\mu'_k}{\sigma'_k})}\right)\right)^2
\end{aligned} \tag{22}$$

Therefore, the variance of the coordinator model's output is:

$$\begin{aligned}
\mathbb{V}_{X_{\mathcal{B}} \in D_{\mathcal{B}}}(f(X_{\mathcal{A}}^*, X_{\mathcal{B}})) &= \mathbb{E}_{X_{\mathcal{B}} \in D_{\mathcal{B}}}(Y^2|Y > 0) \times \mathcal{P}(Y > 0) \\
&\quad - (\mathbb{E}_{X_{\mathcal{B}} \in D_{\mathcal{B}}}(f(X_{\mathcal{A}}^*, X_{\mathcal{B}})))^2 \\
&= \left(\sum_{k=1}^{\mathcal{K}} \pi_k \Phi\left(\frac{\mu'_k}{\sigma'_k}\right)\right) \left(\sum_{k=1}^{\mathcal{K}} \pi_k^2 \sigma_k'^2 \left(1 - \frac{\mu'_k}{\sigma'_k} \frac{\phi(\frac{\mu'_k}{\sigma'_k})}{\Phi(\frac{\mu'_k}{\sigma'_k})} - \left(\frac{\phi(\frac{\mu'_k}{\sigma'_k})}{\Phi(\frac{\mu'_k}{\sigma'_k})}\right)^2\right)\right) \\
&\quad + \left(\sum_{k=1}^{\mathcal{K}} \pi_k \left(\mu'_k + \sigma'_k \frac{\phi(\frac{\mu'_k}{\sigma'_k})}{\Phi(\frac{\mu'_k}{\sigma'_k})}\right)\right)^2 \left(1 - \sum_{k=1}^{\mathcal{K}} \pi_k \Phi\left(\frac{\mu'_k}{\sigma'_k}\right)\right)
\end{aligned} \tag{23}$$

□

E PROOF ON THE EXISTENCE OF ADIS USING BOUNDED MUTATION

In line with the proof given in Sec. 3 by arbitrarily mutating inputs, this section presents the following proof on the existence of ADIS using bounded mutation. Let $X_{\mathcal{A}}^*$ be bounded by a space $\mathcal{S}_{\mathcal{A}}$ in $d_{\mathcal{A}}$ dimension, $X_{\mathcal{A}}^* \in \mathcal{S}_{\mathcal{A}}$. For HeteroLR, μ'_k 's are linear combinations of features in $X_{\mathcal{A}}^*$; therefore, they are also bounded by two limited real numbers: $\mu'_k \in [\mu'_{min}, \mu'_{max}]$. Further, the ratio $\frac{\mu'_k}{\sqrt{\sigma_1^2 + \sigma_k'^2}}$ is bounded by $[r_{min}, r_{max}]$ and the variance is also bounded:

$$\begin{aligned}
\mathbb{V}_{X_{\mathcal{B}} \in D_{\mathcal{B}}}(g(S)) &= \sum_{k=1}^{\mathcal{K}} \frac{\pi_k}{\sqrt{2\pi}} \frac{1}{\sqrt{\sigma_k'^2 + \sigma_2^2}} \exp\left\{-\frac{1}{2} \frac{\mu_k'^2}{\sigma_k'^2 + \sigma_2^2}\right\} \\
&\quad + \sum_{k=1}^{\mathcal{K}} \pi_k \Phi\left(\frac{\mu'_k}{\sqrt{\sigma_1^2 + \sigma_k'^2}}\right) \left(1 - \sum_{k=1}^{\mathcal{K}} \pi_k \Phi\left(\frac{\mu'_k}{\sqrt{\sigma_1^2 + \sigma_k'^2}}\right)\right) \\
&< \sum_{k=1}^{\mathcal{K}} \pi_k \Phi\left(\frac{\mu'_k}{\sqrt{\sigma_1^2 + \sigma_k'^2}}\right) \left(1 - \pi_k \Phi\left(\frac{\mu'_k}{\sqrt{\sigma_1^2 + \sigma_k'^2}}\right)\right) \\
&< \sum_{k=1}^{\mathcal{K}} \pi_k \Phi\left(\frac{\mu'_k}{\sqrt{\sigma_1^2 + \sigma_k'^2}}\right) - \frac{1}{\mathcal{K}} \left(\sum_{k=1}^{\mathcal{K}} \pi_k \Phi\left(\frac{\mu'_k}{\sqrt{\sigma_1^2 + \sigma_k'^2}}\right)\right)^2 \\
&< \Phi(r_{max}) - \frac{1}{\mathcal{K}} \Phi(r_{max})^2
\end{aligned} \tag{24}$$

If r_{max} satisfies $\Phi(r_{max}) \leq \frac{\mathcal{K} + \sqrt{\mathcal{K}^2 - 4\epsilon\mathcal{K}}}{2}$, the variance must be bounded by ϵ , $\mathbb{V}_{X_{\mathcal{B}} \in D_{\mathcal{B}}}(Sigmoid(S)) \leq \epsilon$, which means the ADI $X_{\mathcal{A}}^*$ generated by bounded mutation exists.

Similarly, for SplitNN, μ'_k 's are also bounded, $\mu'_k \in [\mu'_{min}, \mu'_{max}]$. Similarly, $\sigma'_k \in [\sigma'_{min}, \sigma'_{max}]$ and $\frac{\mu'_k}{\sigma'_k} \in [r_{min}, r_{max}]$. When $\mu'_k \leq 0$, the variance is thus bounded by:

$$\begin{aligned}
\mathbb{V}_{X_{\mathcal{B}} \in D_{\mathcal{B}}}(f(X_{\mathcal{A}}^*, X_{\mathcal{B}})) &= \mathbb{E}_{X_{\mathcal{B}} \in D_{\mathcal{B}}}(Y^2|Y > 0) \times \mathcal{P}(Y > 0) \\
&\quad - (\mathbb{E}_{X_{\mathcal{B}} \in D_{\mathcal{B}}}(f(X_{\mathcal{A}}^*, X_{\mathcal{B}})))^2 \\
&= (\mathbb{E}_{X_{\mathcal{B}} \in D_{\mathcal{B}}}(Y|Y > 0))^2 \times \mathcal{P}(Y > 0) (1 - \mathcal{P}(Y > 0)) \\
&\quad + \mathbb{V}_{X_{\mathcal{B}} \in D_{\mathcal{B}}}(Y|Y > 0) \times \mathcal{P}(Y > 0)
\end{aligned} \tag{25}$$

$$\begin{aligned}
&\leq \mathbb{V}_{X_{\mathcal{B}} \in D_{\mathcal{B}}}(Y|Y > 0) \times \Phi(r_{max}) + \frac{1}{4} (\mathbb{E}_{X_{\mathcal{B}} \in D_{\mathcal{B}}}(Y|Y > 0))^2 \\
&< \Phi(r_{max}) + \frac{1}{4} \Phi(r_{max}) \mu_{min}'^2 + \frac{1}{4} \mu_{max}'^2 + \frac{1}{4} \sigma_{max}'^2 \frac{\phi(r_{max})^2}{\Phi(r_{min})^2}
\end{aligned}$$

If the boundaries satisfy:

$$\Phi(r_{max}) + \frac{1}{4} \Phi(r_{max}) \mu_{min}'^2 + \frac{1}{4} \mu_{max}'^2 + \frac{1}{4} \sigma_{max}'^2 \frac{\phi(r_{max})^2}{\Phi(r_{min})^2} \leq \epsilon \tag{26}$$

, then the variance must be bounded by ϵ : $\mathbb{V}_{X_{\mathcal{B}} \in D_{\mathcal{B}}}(f(x_{\mathcal{A}}^*, x_{\mathcal{B}})) \leq \epsilon$. Thus, the ADI $X_{\mathcal{A}}^*$ generated by bounded mutation exists.

F COOPERATING FUZZ TESTING WITH VFL PROTOCOLS

As reported in Sec. 7, we launch fuzz testing toward two widely-used VFL protocols (i.e. HeteroLR and SplitNN) on the basis of real-world VFL platforms FATE and FedML. We also launch fuzz testing toward VFVQA, whose protocol is consistent with SplitNN. A detailed procedure to cope with fuzz testing with learning protocols is given in Table 9. In all, greybox fuzzing can be accordingly performed on the distributed versions of learning protocols without sharing much information about the original data.

G DATASETS INFORMATION

We use five popular datasets in our evaluation Sec. 7: NUS-WIDE [22], Credit [1], Vehicle [5], MNIST [45], and VQA v2.0 [50]. The NUS-WIDE dataset contains 269,648 images and the associated tags. Each sample has 634 low-level image features and 1,000 text features. Thus, it is suitable for a feature-partition setting and is therefore commonly used to benchmark VFL. We set up a joint classification task of ten labels via two participants \mathcal{A} and \mathcal{B} . We choose the top ten labels in NUS-WIDE having the maximum number of data samples. \mathcal{A} holds the image features whereas \mathcal{B} holds the text features.

The Credit dataset is a popular benchmark dataset for VFL that comprises the payment records of 30,000 customers of a bank, where 5,000 customers are malicious while the rest are benign. Each data sample has 23 integer or floating-point number features. We set up a VFL logistic regression task over participants \mathcal{A} and \mathcal{B} to predict whether a payment is from a malicious customer or not. Participant \mathcal{A} holds 13 features and participant \mathcal{B} holds 10.

The Vehicle dataset is a multi-classification dataset containing 946 samples of four vehicle categories. Each sample has 18 features. We set up a VFL logistic regression task over two participants \mathcal{A} and \mathcal{B} to classify data samples into the vehicle categories. Both \mathcal{A} and \mathcal{B} get nine features each.

Table 9: Detail steps to cooperate fuzz testing with the VFL protocols.

	Participant \mathcal{A}	Participant \mathcal{B}	Coordinator \mathcal{C}
1.	Generate index Seeds \mathcal{S} , maintain a list \mathcal{Q} storing the corresponding data.	Compute all local results of data in participant \mathcal{B} , send to \mathcal{C}	
2.	a) Choose next from \mathcal{S} as $index_a$. b) Add noise to $\mathcal{Q}[index_a]$ for β times. c) Compute local results of the noised data, send to \mathcal{C} .		
3.			a) Randomly choose a local result of participant \mathcal{B} and the corresponding index is $index_b$. b) Compute the outputs of all noised data and gradients, send to \mathcal{A} and \mathcal{B} .
4.	Compute the saliency score of all noised data, send the highest $saliency_score_a$ and corresponding $index_noise_a$ to \mathcal{C} .	Compute the $saliency_score_orig_b$, send to \mathcal{C} .	
5.			Compute Attack Success Rate, send to \mathcal{A} .
6.	a) Maintain the $orig_acc$. b) Compute the Saliency Mask based on the gradients received. c) Compute $data_noise_mask_a$ based on the Mask. d) Compute the local result of $data_noise_mask_a$, send to \mathcal{C} .		
7.			Compute output, gradients and Attack Success Rate ($masked_acc$), send to \mathcal{A} and \mathcal{B} .
8.	Compute $saliency_score_masked_a$, send to \mathcal{C} .	Compute $saliency_score_masked_b$, send to \mathcal{C} .	
9.			Compute $ratio_a = saliency_score_masked_a / saliency_score_orig_a$ and $ratio_b = saliency_score_masked_b / saliency_score_orig_b$, send to \mathcal{A} .
10.	If $masked_acc > orig_acc$ and $ratio_a > ratio_b$, update $\mathcal{Q}[index_a] = data_noise_mask_a$. If $masked_acc > threshold$, add $\mathcal{Q}[index_a]$ to \mathcal{A} , delete $index_a$ from \mathcal{S} and return to Step 2.		
11.	Return to step 3 for γ times.		
12.	Return to step 2 for Γ times.		

MNIST is a handwritten digital image dataset with 60,000 training samples and 10,000 testing samples, each with dimensions of 28×28 pixels. We set up a VFL classification task with ten labels over participants \mathcal{A} and \mathcal{B} . Each image is vertically partitioned into two such that \mathcal{A} gets the left piece (with 28×14 pixels) while \mathcal{B} gets the right piece.

VQA v2.0 is a large-scale dataset widely used to train VQA models. We set up VFVQA over participants \mathcal{A} and \mathcal{B} to facilitate VQA, where \mathcal{A} holds images and \mathcal{B} raises natural-language questions. There are 82,783 images and 443,757 questions in the training set, and 40,504 images and 214,354 questions in the validation set. The images are embedded as a feature vector of size 2,054 while the questions are embedded as a word embedding matrix with shape 128×512 .

H FUZZ TESTING & BLACKBOX EXTENSION RESULTS VISUALIZATION

The ADIs generated by fuzz testing and original inputs of participant \mathcal{A} are projected to 2D figures by multidimensional scaling. As shown in Fig. 14, the ADIs are distributed close to the original data. We interpret that the generated ADIs (marked in red) are *stealthy*: they can be hardly distinguished by the data distribution nor by the distances between the data points directly.

We also present several MNIST cases generated by fuzz testing in Fig. 15. Similar to Fig. 7, we report the ADIs used by \mathcal{A} , the normal inputs used by \mathcal{B} , and also the corresponding saliency maps. It is easy to see that ADIs on \mathcal{A} dominate the joint inference, and make the contribution of \mathcal{B} negligible.

In addition to MNIST (Fig. 6) synthesized using our gradient-based whitebox algorithm, Fig. 16 shows MNIST images generated using the blackbox algorithm presented in Sec. 4. The synthesized ADIs in Fig. 16, after concatenating with the right half of arbitrary MNIST images, control the joint inference to fixed labels (i.e., the

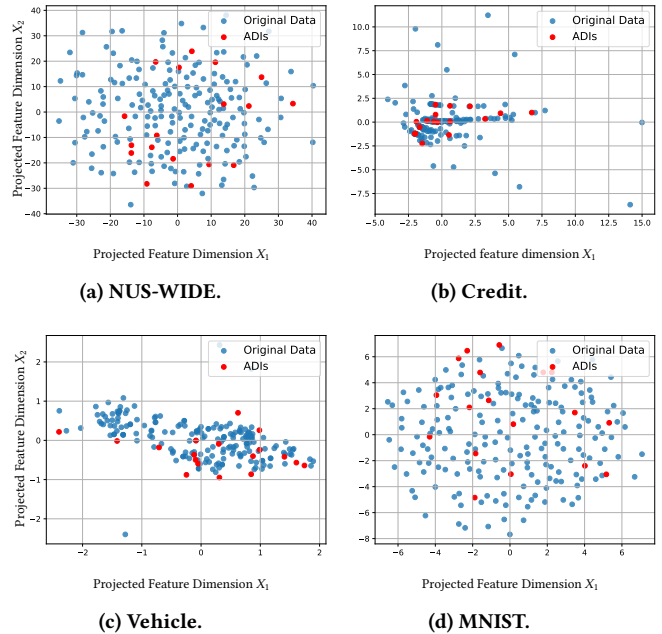


Figure 14: Normal inputs and ADIs generated by fuzz testing projected to 2D figures.

last column) determined by adversaries. We view this as convincing to empirically illustrate the effectiveness of our blackbox attack.

I REWARDS ESTIMATION

Several schemes are proposed to analyze the fairness and rewarding in federated learning and collaborative machine learning [72–74, 90, 91]. Despite the difference in implementations, they primarily assess the importance of a participant’s contribution in a joint

ADI From \mathcal{A} / Normal Inputs From \mathcal{B}	Expectation of \mathcal{B}	Joint Inference Results
	1	8
	7	3
	0	7
	6	3
	5	8

Figure 15: ADIs found in MNIST using fuzz testing.

\mathcal{A} 's Input Images Before/After Mutation	Images Input in \mathcal{B}	Joint Inference Results
		6
		7
		8
		2
		3

Figure 16: ADIs found in MNIST using the blackbox attack.

Table 10: Contribution Estimation.

		\mathcal{A}	\mathcal{B}
NUS-WIDE	Normal Inputs Used by Both Sides	0.492	0.508
	ADIs in \mathcal{A} , Normal Inputs in \mathcal{B}	0.859	0.141
Credit	Normal Inputs Used by Both Sides	0.457	0.543
	ADIs in \mathcal{A} , Normal Inputs in \mathcal{B}	0.856	0.144
Vehicle	Normal Inputs Used by Both Sides	0.504	0.496
	ADIs in \mathcal{A} , Normal Inputs in \mathcal{B}	0.784	0.216
MNIST	Normal Inputs Used by Both Sides	0.429	0.571
	ADIs in \mathcal{A} , Normal Inputs in \mathcal{B}	0.833	0.167
VQA v2.0	Normal Inputs Used by Both Sides	0.279	0.721
	ADIs in \mathcal{A} , Normal Inputs in \mathcal{B}	0.352	0.648

prediction. The VFL frameworks we evaluated do not offer an “out-of-the-box” rewarding estimation module. Therefore, to estimate rewards for each participant in a joint inference, we take a general approach to measuring the L^1 norm of the saliency map (line 3 in Alg. 1) derived from each participant’s input data.

Table 10 reports the normalized estimated rewards for different datasets. To generate ADIs, we use bounded mutation under the 95% threshold. It is easy to see that given normal inputs used by both ends, each participant is estimated to receive approximately the same reward (except VFVQA; see discussion below). For instance, given one unit of reward offered for each joint inference over the NUS-WIDE dataset, participants \mathcal{A} and \mathcal{B} anticipate receiving 0.492

and 0.508 units of rewards, respectively. In contrast, when \mathcal{A} uses ADIs, \mathcal{A} can receive 0.859 units of rewards for at least 95% of joint inferences. This is consistent with our discussion in Sec. 3.2.

For VQA v2.0, we also observed that the contribution of \mathcal{B} drops when \mathcal{A} uses ADIs. However, we clarify that results in Table 10 indeed *underestimate* the dominance of ADIs. Recall for this VFVQA task, \mathcal{B} raises natural-language questions toward images possessed by \mathcal{A} . The gradients of natural-language question inputs in VFVQA measure the *local* sensitivity of the VFVQA system. However, different from other tasks, the perturbed questions will not form reasonable text if they are only perturbed by gradients measuring local sensitivity. This also explains why the contribution of \mathcal{B} in Table 10, even for normal inputs, seems larger than \mathcal{A} .

While there exist some works on quantifying the attention of either natural-language questions or images [42, 53], it’s generally an open problem to compare the contribution of images and natural-language questions in an apple-to-apple manner. We follow [36] to approximate and compare the contributions of images and questions particularly in the VFVQA settings. Overall, the approach proposed by [36] is conceptually consistent with our evaluation in Sec. 7, where the questions or images are replaced by other data samples in the dataset to see how these replacements will influence the joint inference. We report that when using this method to compare the contributions of \mathcal{A} and \mathcal{B} , \mathcal{A} and \mathcal{B} will get 0.511 and 0.489 units of rewards on average when both participants use normal inputs. In contrast, when \mathcal{A} uses ADIs, \mathcal{A} will hog all the rewards.